Equation of state of nucleon matter and neutron star structure

A. Akmal,* V. R. Pandharipande,† and D. G. Ravenhall‡
Department of Physics, University of Illinois at Urbana-Champaign, 1110 West Green Street, Urbana, Illinois 61801
(Received 14 April 1998)

Properties of dense nucleon matter and the structure of neutron stars are studied using variational chain summation methods and the new Argonne v_{18} two-nucleon interaction, which provides an excellent fit to all of the nucleon-nucleon scattering data in the Nijmegen database. The neutron star gravitational mass limit obtained with this interaction is $1.67M_{\odot}$. Boost corrections to the two-nucleon interaction, which give the leading relativistic effect of order $(v/c)^2$, as well as three-nucleon interactions, are also included in the nuclear Hamiltonian. Their successive addition increases the mass limit to 1.80 and 2.20 $M_{\odot}$. Hamiltonians including a three-nucleon interaction predict a transition in neutron star matter to a phase with neutral pion condensation at a baryon number density of ~ 0.2 fm^{-3}. Neutron stars predicted by these Hamiltonians have a layer with a thickness on the order of tens of meters, over which the density changes rapidly from that of the normal to the condensed phase. The material in this thin layer is a mixture of the two phases. We also investigate the possibility of dense nucleon matter having an admixture of quark matter, described using the bag model equation of state. Neutron stars of $1.4M_{\odot}$ do not appear to have quark matter admixtures in their cores. However, the heaviest stars are predicted to have cores consisting of a quark and nucleon matter mixture. These admixtures reduce the maximum mass of neutron stars from 2.20 to 2.02 (1.91) $M_{\odot}$ for bag constant $B=200$ (122) MeV/fm^3. Stars with pure quark matter in their cores are found to be unstable. We also consider the possibility that matter is maximally incompressible above an assumed density, and show that realistic models of nuclear forces limit the maximum mass of neutron stars to be below $2.5M_{\odot}$. The effects of the phase transitions on the composition of neutron star matter and its adiabatic index Γ are discussed. [S0556-2813(98)04509-9]

PACS number(s): 21.65.+f, 26.60.+c, 97.60.Jd

I. INTRODUCTION

The significant influence of nuclear forces on neutron star structure is by now firmly established by a large body of theoretical and observational evidence [1]. In the absence of these forces, the maximum possible mass of neutron stars composed of noninteracting neutrons is ~ 0.7 solar masses ($M_{\odot}$) [2]. Since most observed neutron star masses are above $1.3M_{\odot}$ [3], they must be supported against gravitational collapse by pressure originating from nuclear forces. In the present work, we study neutron star structure using one of the most realistic models of nuclear forces currently available. A brief outline of previous calculations leading to this work is presented below.

Shortly after the discovery of pulsars, calculations of the equation of state (EOS) of neutron star matter with realistic models of the two nucleon interaction (NNI), obtained by fitting the nucleon-nucleon (NN) scattering data then available, were carried out using the lowest order constrained variational method [4,5]. The results demonstrated that nuclear forces increase the mass limit of stable neutron stars beyond $1.4M_{\odot}$.

By the late 1970s it had become clear that the NNI alone could not account for the properties of nuclear matter or few-body nuclei. Variational [6] and Brueckner calculations [7], including higher order cluster contributions, established that nuclear matter with realistic NNI saturates at too high a density. In addition, these interactions were known to underbind ^{3}H. Ignoring the latter problem, plausible density dependent terms were added to the Urbana v_{14} (U14) model of NNI [8,9] to reproduce the observed equilibrium properties of nuclear matter. The resulting density dependent (U14-DDI) model of nuclear forces predicted stable neutron stars having masses up to $1.8M_{\odot}$ [10,11].

Since nucleons are made up of quarks and have internal degrees of freedom, we can expect interactions among three (and perhaps four or more) nucleons, in addition to the NNI. The Urbana three nucleon interaction (TNI) models contain only two terms, with strengths fixed by the saturation density of nuclear matter and the binding energy of ^{3}H. Wiringa, Fiks, and Fabrocini (WFF) [12] used the U14 and the subsequent Argonne v_{14} (A14) [13] models of NNI, together with the Urbana VII (UVII) model of TNI, to study neutron star structure and obtained mass limits of $2.19M_{\odot}$ and $2.13M_{\odot}$ with the U14+UVII and A14+UVII, respectively. They also found that pure neutron matter (PNM) undergoes a transition to a phase having spin-isospin order, attributed to neutral pion condensation, at a density of ~ 0.2 fm^{-3} with the A14 +UVII, but not with the U14+UVII. Neither of these models results in a phase transition in symmetric nuclear matter (SNM), which is composed of equal numbers of neutrons and protons.

In the early 1990s the Nijmegen group [14] examined carefully all NN scattering data at energies below 350 MeV published between 1955 and 1992. They extracted 1787 proton-proton (pp) and 2514 proton-neutron (np) ''reliable'' data, and demonstrated that these data determine all NN

*Electronic address: akmal@rsm1.physics.uiuc.edu
†Electronic address: vrp@uiuc.edu
‡Electronic address: ravenhal@uiuc.edu

phase shifts and mixing parameters quite accurately. The NNI models which fit this Nijmegen database with a $\chi^2/N_{data} \sim 1$ are called ''modern.'' These include the Nijmegen models [15]: Nijmegen I, II and Reid-93, the Argonne v_{18} [16], denoted here by A18, and the CD-Bonn [17]. In order to fit the pp and np data simultaneously and accurately, these models include a detailed description of the electromagnetic interactions and terms that break the isospin symmetry of nuclear forces. All include the long range one-pion exchange potential, but follow different treatments of the intermediate and short range parts of the NNI. The differences among the predictions of these models for the properties of many-body systems are much smaller than those among the predictions of older models, presumably because all modern potentials accurately fit the same scattering data. For example, the ^{3}H binding energies predicted by the modern Nijmegen models and A18 are between -7.62 to -7.72 MeV [18], while that of CD-Bonn is -8.00 MeV [17]. The difference between these results and the experimental value of -8.48 MeV is used to fix one of the parameters of Urbana TNI models.

Detailed studies of the energies of dense nucleon matter were carried out recently by Engvik *et al.* [19] using all the modern models of NNI and the lowest order Brueckner (LOB) method. According to these studies, the results with the modern potentials are all quite similar up to densities relevant to neutron stars. For example, the energies predicted with the LOB method for neutron matter at $5\rho_0$, where $\rho_0 = 0.16$ fm^{-3} is the equilibrium (saturation) density of nuclear matter, range from 80 to 93 MeV per nucleon. The spread of 13 MeV in these energies is small compared to the possible errors in the LOB method and the expected contributions of TNI at this density. This model independence results from the fact that the mean interparticle distance at $\rho \sim 5\rho_0$ is greater than 1 fm, and the predicted matter energy is therefore not sensitive to the details of the interaction at $r_{ij} < 1$ fm.

In this paper we study the structure of neutron stars with the A18 model using variational chain summation (VCS) methods, which hopefully include all leading many-body correlation effects. The Urbana model IX (UIX) [20] is used to estimate the effect of TNI. Previous studies of nucleon matter with A18 and UIX interactions have indicated the possibility of a transition to a neutral pion condensed phase for both PNM and SNM [21]. The effects of such a transition on the structure of neutron stars are studied here in detail. The effect of relativistic boost corrections [22] to the A18 interaction is also examined. At high densities, we consider the possibility of matter becoming maximally incompressible, as well as that of a transition to mixed phases of quark and nucleon matter [23,24].

The relativistic mean field (RMF) approximation [25] has been used in many studies of high density matter and neutron stars. There exists a vast amount of literature on this topic, some of which has been reviewed by Glendenning [26]. While the RMF approximation is very elegant and pedagogically useful, it is not valid in the context of what is known about nuclear forces, which is the theme of this work. For example, using the meson parameters of the CD-Bonn S-wave potentials in the RMF approximation leads to unbound SNM. (In order to accurately fit the NN scattering data, the phenomenological scalar meson parameters in the CD-Bonn model are allowed to depend on partial wave quantum numbers.) At a density of ρ_0, for SNM, the RMF approximation yields an energy per nucleon of $\sim +20$ MeV, while the LOB method gives ~ -18 MeV. In the mean field Hartree approximation, which is implicit in the RMF calculations, the A18 NNI gives energies per nucleon of $\sim +30$ $(+37)$ MeV at ρ_0 and $+155$ $(+204)$ MeV at $5\rho_0$ for SNM (PNM), while the variational calculations presented here give ~ -18 $(+12)$ and $+25$ $(+88)$ MeV, respectively.

The main problem is that the mean field approximation for meson fields is only valid for $\mu\bar{r} \ll 1$, where μ is the inverse Compton wavelength of the meson and $\bar{r}$ is the mean interparticle spacing. Over the 1-5 ρ_0 density range, $\bar{r}$ estimated using a body centered cubic lattice ranges from 2 to 1.2 fm. Thus $\mu\bar{r}$ is in the range 1.4 to 0.8 for the pion and 7.8 to 4.7 for vector mesons. The mean field approximation is not applicable, since these values are obviously far from being much smaller than one. The RMF approximation can be based on effective values of the coupling constants that take into account the correlation effects. However, these coupling constants then have a density dependence, and a microscopic theory is needed to calculate them.

This paper is organized as follows. Section II contains a summary of the nonrelativistic calculations with A18 and A18+UIX models of nuclear forces, while Sec. III describes the calculations including the relativistic boost interaction, denoted by δv, without and with the TNI model UIX*. The beta equilibrium of neutron star matter is discussed in Sec. IV and results for neutron star structure are presented in Sec. V, where we also discuss the effects of the possible transition to mixed nucleon and quark matter phases. The adiabatic index and sound velocities in neutron star matter are given in Sec. VI, and conclusions are presented in Sec. VII.

II. NONRELATIVISTIC CALCULATIONS

Nonrelativistic calculations of SNM and PNM with the A18 and UIX interactions were carried out using variational chain summation (VCS) techniques described in detail in [21]. Energies are calculated by evaluating the expectation value of the Urbana-Argonne Hamiltonian with a variational wave function composed of a product of pair correlation operators acting on a Fermi gas wave function. The pair correlation operators are written as a sum of eight radial correlation functions, each multiplied by one of the two-body operators: $(1, \boldsymbol{\sigma}_i \cdot \boldsymbol{\sigma}_j, S_{ij}, (\mathbf{L}\cdot\mathbf{S})_{ij}) \otimes (1, \boldsymbol{\tau}_i \cdot \boldsymbol{\tau}_j)$. The wave function depends on three variational parameters: the range of the tensor correlations, d_t, the range of all other correlations, d_c, and a quenching parameter α, meant to simulate medium effects. In this section we discuss results obtained for four cases, namely SNM and PNM with and without the three-nucleon interaction, in order to indicate their sensitivity to various terms in the nuclear force, and to extend them to higher densities, beyond the range covered in [21].

The optimum values of the parameters d_t and d_c in matter without and with the three-nucleon interaction are shown in Fig. 1. Some of the noise in the variation of these parameters with matter density is due to the insensitivity of the energy to their values at the variational minimum. The large increase

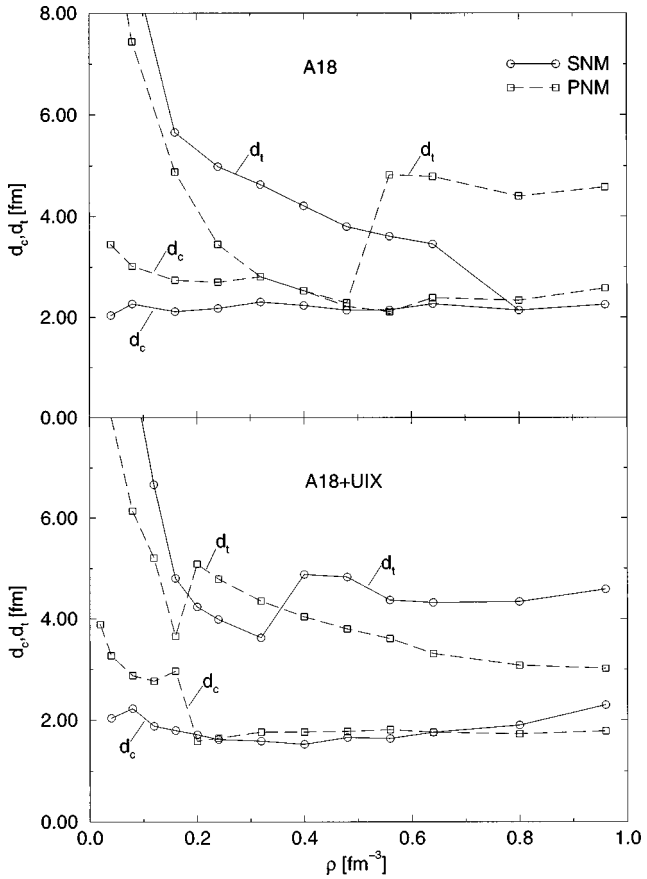

FIG. 1. Central and tensor healing distances (d_c and d_t), for SNM and PNM, with A18 interaction alone (upper graph), and with A18+UIX interaction (lower graph).

in d_t of PNM without V_{ijk} at $\rho \sim 0.5$ fm^{-3} is due to a transition to a phase with π^0-condensation as discussed in [21]. With V_{ijk} there are sudden changes in the d_c and d_t of PNM at $\rho \sim 0.2$ fm^{-3}, and in the d_t of SNM at $\rho \sim 0.32$ fm^{-3}. These are associated with the same phase transition. We note that the present variational wave function is not fully adequate to describe the long range order in the π^0-condensed phases. However, since the change in the energy due to the π^0-condensation appears to be small, we expect our estimates of the energies of matter with π^0-condensation to be useful.

Our nonrelativistic Hamiltonian, H_{NR}, is comprised of the nonrelativisic kinetic energies and the two-body A18 and three-body UIX interactions. The NNI includes a static, long-range one-pion exchange part, with short-range cutoff, and phenomenological intermediate and short-range parts, which depend on the six static two-body operators $(1,\boldsymbol{\sigma}_i\cdot\boldsymbol{\sigma}_j,S_{ij})\otimes(1,\boldsymbol{\tau}_i\cdot\boldsymbol{\tau}_j)$ and eight momentum-dependent (MD) two-body operators: $((\mathbf{L}\cdot\mathbf{S})_{ij}, L^2_{ij}, \boldsymbol{\sigma}_i\cdot\boldsymbol{\sigma}_j L^2_{ij}, (\mathbf{L}\cdot\mathbf{S})^2_{ij}) \otimes(1,\boldsymbol{\tau}_i\cdot\boldsymbol{\tau}_j)$. The A18 includes an additional isovector operator, and three isotensor operators, which distinguish between pp, np and nn interactions. These isovector and isotensor terms are small, and give zero contribution to the energy of SNM to first order. They are therefore neglected in SNM calculations. In the case of PNM all the isospin operators can be eliminated and the full A18 with isovector and isotensor terms becomes the sum of a static part with operators $(1,\boldsymbol{\sigma}_i\cdot\boldsymbol{\sigma}_j,S_{ij})$, and a MD part with operators $(\mathbf{L}\cdot\mathbf{S})_{ij}$, $L^2_{ij}, \boldsymbol{\sigma}_i\cdot\boldsymbol{\sigma}_j L^2_{ij}$ and $(\mathbf{L}\cdot\mathbf{S})^2_{ij}$. The UIX model of V_{ijk} contains two static terms; the two-pion exchange Fujita-Miyazawa interaction, $V^{2\pi}_{ijk}$, and a phenomenological, intermediate range repulsion V^{R}_{ijk}. The strength of the $V^{2\pi}_{ijk}$ interaction was determined by reproducing the binding energy of the triton via Green's-function Monte Carlo (GFMC) calculations [20], while that of V^{R}_{ijk} was adjusted to reproduce the saturation density of SNM.

Expectation values of the various interactions are calculated in the VCS framework by summing terms in their cluster expansions. The one-body, two-body, and many-body contributions to the kinetic and NNI energies are listed in Tables I–IV. The one-body cluster contribution includes only the Fermi gas kinetic energy, T_F. The remainder of the kinetic energy is separated into the contribution from the two-body cluster $\langle T\rangle_{2B}$ and that coming from the many-body clusters, $\langle T\rangle_{MB}$. The kinetic energy can be calculated using different expressions related by integration by parts. If all MB contributions are calculated, these expressions yield the same result. However, they yield different results when only selected parts of the MB clusters are summed by VCS techniques. We have calculated the many-body kinetic energy using expressions due to Pandharipande and Bethe (PB), and to Jackson and Feenberg (JF) [27]. The averages of the PB and JF results appear under the column $\langle T\rangle_{MB}$, and the differences $T_{PB}-T_{JF}$ are listed under ΔT. In studies of atomic helium liquids the exact energies, calculated via Monte Carlo

TABLE I. Cluster contributions to A18 SNM $E(\rho)$ in MeV.

ρ	T_F	$\langle T\rangle_{2B}$	$\langle T\rangle_{MB}$	ΔT	$\langle v^s\rangle_{2B}$	$\langle v^{MD}\rangle_{2B}$	$\langle v^s\rangle_{MB}$	$\langle v^{MD}\rangle_{MB}$	δE_{2B}
0.04	8.77	5.33	−0.29	0.16	−19.46	0.03	1.43	0.17	−0.27
0.08	13.93	10.30	−1.06	0.47	−36.84	0.43	4.44	0.64	−0.57
0.16	22.11	19.64	−1.79	1.11	−66.48	2.04	8.44	2.58	−1.13
0.24	28.97	26.95	−2.47	1.49	−91.46	4.69	12.06	5.39	−1.73
0.32	35.09	34.45	−3.92	1.63	−115.82	7.89	17.17	9.37	−2.37
0.40	40.72	40.55	−3.23	1.53	−135.38	11.96	17.57	14.48	−3.03
0.48	45.99	46.22	−1.95	1.17	−152.83	16.69	16.55	20.76	−3.63
0.56	50.96	51.95	−1.82	0.46	−170.59	21.72	17.92	28.24	−4.17
0.64	55.71	58.03	−3.73	−0.99	−188.73	26.61	22.56	36.91	−4.60
0.80	64.64	68.60	4.47	−4.07	−202.42	34.67	8.42	51.76	−5.13
0.96	73.00	79.71	−0.40	−8.27	−236.38	47.43	18.47	80.12	−5.43

TABLE II. Cluster contributions to A18 PNM $E(\rho)$ in MeV.

ρ	T_F	$\langle T\rangle_{2B}$	$\langle T\rangle_{MB}$	ΔT	$\langle v^s\rangle_{2B}$	$\langle v^{MD}\rangle_{2B}$	$\langle v^s\rangle_{MB}$	$\langle v^{MD}\rangle_{MB}$	δE_{2B}
0.04	13.92	5.08	−1.93	0.14	−15.79	0.41	4.90	−0.14	−0.39
0.08	22.09	8.21	−2.49	0.26	−26.87	1.34	6.92	−0.22	−0.46
0.16	35.07	15.00	−3.02	0.43	−48.10	4.15	9.75	0.28	−0.80
0.24	45.95	21.67	−2.89	0.20	−67.45	7.67	11.01	1.92	−1.20
0.32	55.67	28.50	−3.65	−0.54	−86.52	11.95	12.81	5.16	−1.73
0.40	64.60	31.71	−0.28	−1.07	−98.77	17.57	6.97	9.95	−2.33
0.48	72.95	37.39	4.57	−1.23	−113.39	23.89	0.93	15.57	−3.00
0.56	80.84	43.86	3.15	7.25	−141.33	35.90	−1.98	32.50	−3.86
0.64	88.37	56.20	0.99	8.55	−168.18	40.75	0.50	45.53	−4.80
0.80	102.54	67.08	2.35	5.72	−201.26	57.99	−6.50	73.07	−7.00
0.96	115.80	80.44	−2.75	2.83	−237.50	74.78	−8.05	112.66	−10.08

(MC) methods, lie between the PB and JF values evaluated using VCS methods [28]. Although exact MC calculations are as yet not practical for nucleon matter, we believe the average of the two expressions to be more accurate than either one, and that the difference provides a measure of the uncertainty in the many-body calculation. The $\langle T\rangle_{MB}$ is quite small in nucleon matter, due to cancellations between various many-body terms, and therefore the difference ΔT is a better indication of this uncertainty.

The two-body cluster contribution to the static and MD parts of the NNI energy are listed under $\langle v^s\rangle_{2B}$, and $\langle v^{MD}\rangle_{2B}$. The $\langle v^s\rangle_{2B}$ is negative and large enough to bind SNM, though not PNM. The $\langle v^{MD}\rangle_{2B}$ increases rapidly with density, and is proportional to ρT_F at $\rho > 2\rho_0$. The many-body contributions to the static and MD parts of the NNI energy are listed separately as $\langle v^s\rangle_{MB}$ and $\langle v^{MD}\rangle_{MB}$. Previously, great efforts were made to improve upon the accuracy of the calculation of $\langle v^s\rangle_{MB}$ [6,29]; however, at large densities the $\langle v^{MD}\rangle_{MB}$ grows rapidly, and becomes larger in magnitude than $\langle v^s\rangle_{MB}$. The MD contribution is more difficult to calculate because of the gradients in v_{ij}^{MD}, which may operate on the correlations of nucleons i and j with other nucleons. All the leading terms are calculated as discussed in [21], and the corresponding errors should therefore be much smaller than the reported values. At higher densities the $\langle v^{MD}\rangle_{MB}$ becomes proportional to $\rho\langle T\rangle_{2B}$, as expected. An additional perturbative correction to the two-body energy is listed as δE_{2b}. This small correction is due to an improvement in the variational wave function, which occurs when correlation functions are calculated separately in each l,S,J channel [21].

The expectation values of v_{ij}^{π}, v_{ij}^{R}, $V_{ijk}^{2\pi}$, and V_{ijk}^{R} for SNM and PNM are listed in Table V. Here, v_{ij}^{R} is the phenomenological part, $v_{ij}-v_{ij}^{\pi}$, of the NNI. Since the UIX V_{ijk} is purely static, the error in the calculation of its expectation value is likely to be small. In SNM, with only the A18 interaction, the v^{π} gives more than half of the total NNI energy at all densities considered. The corresponding calculation with A18+UIX interactions shows a significant increase in the magnitudes of the negative contribution of $V_{ijk}^{2\pi}$ between $\rho = 0.32$ and 0.4 fm^{-3} associated with pion condensation. In PNM these pion exchange interactions make relatively small contributions at densities below the phase transition, occurring at $\rho \sim 0.2$ (0.5) fm^{-3} with (without) UIX. However, at the densities above the transition they make large negative contributions comparable to those in SNM. At the highest densities the contributions of $V_{ijk}^{2\pi}$ and V_{ijk}^{R} become very large, and the validity of this purely nonrelativistic approach becomes questionable. As discussed in

TABLE III. Cluster contributions to A18+UIX SNM $E(\rho)$ in MeV.

ρ	T_F	$\langle T\rangle_{2B}$	$\langle T\rangle_{MB}$	ΔT	$\langle v^s\rangle_{2B}$	$\langle v^{MD}\rangle_{2B}$	$\langle v^s\rangle_{MB}$	$\langle v^{MD}\rangle_{MB}$	δE_{2B}
0.04	8.77	5.70	−0.34	0.19	−20.00	−0.01	1.60	0.19	−0.28
0.08	13.93	10.16	−0.97	0.46	−36.51	0.44	4.21	0.64	−0.60
0.12	18.25	15.27	−0.74	0.89	−51.63	1.24	5.25	1.60	−1.10
0.16	22.11	20.97	−0.81	1.21	−66.74	2.12	6.52	3.01	−1.80
0.20	25.65	25.84	−0.46	1.51	−80.18	3.47	7.12	4.77	−2.54
0.24	28.97	30.51	0.22	1.87	−93.16	5.38	7.51	7.10	−3.33
0.32	35.09	39.38	1.32	2.46	−117.90	9.41	8.60	12.56	−5.21
0.40	40.72	53.32	0.54	6.24	−154.44	15.18	23.65	25.65	−6.93
0.48	45.99	61.13	1.08	7.80	−178.46	18.79	27.12	34.34	−7.93
0.56	50.96	69.68	2.27	8.51	−201.66	24.75	27.70	45.69	−8.67
0.64	55.71	79.46	1.92	10.20	−227.19	28.60	32.93	58.95	−9.20
0.80	64.64	93.07	1.71	12.89	−269.82	39.35	39.57	87.26	−9.73
0.96	73.00	111.43	−6.19	18.52	−321.23	48.48	61.29	128.26	−9.93

TABLE IV. Cluster contributions to A18+UIX PNM $E(\rho)$ in MeV.

ρ	T_F	$\langle T\rangle_{2B}$	$\langle T\rangle_{MB}$	ΔT	$\langle v^s\rangle_{2B}$	$\langle v^{MD}\rangle_{2B}$	$\langle v^s\rangle_{MB}$	$\langle v^{MD}\rangle_{MB}$	δE_{2B}
0.02	8.77	3.89	−1.66	0.08	−10.20	0.11	3.70	−0.06	−0.23
0.04	13.92	5.15	−1.77	0.14	−15.60	0.38	4.53	−0.14	−0.42
0.08	22.09	8.43	−2.25	0.30	−26.69	1.27	6.37	−0.23	−0.83
0.12	28.95	11.97	−2.70	0.42	−37.77	2.51	8.22	−0.14	−1.13
0.16	35.07	15.90	−4.00	0.18	−49.36	3.87	11.44	0.04	−1.26
0.20	40.69	22.37	0.42	2.78	−59.04	10.65	3.40	4.87	−1.29
0.24	45.95	25.45	1.15	3.25	−69.41	13.03	2.89	6.32	−1.65
0.32	55.67	35.82	2.49	4.44	−93.04	18.04	2.48	11.04	−2.45
0.40	64.60	42.87	4.34	5.38	−113.78	25.07	0.31	16.94	−3.20
0.48	72.95	51.57	6.35	6.27	−135.45	32.61	−2.18	24.67	−4.00
0.56	80.84	61.73	8.57	7.07	−157.94	40.68	−4.92	34.25	−4.75
0.64	88.37	80.34	12.00	7.62	−185.72	53.35	−8.56	47.64	−5.45
0.80	102.54	101.95	18.33	7.90	−230.35	77.63	−16.19	74.42	−6.50
0.96	115.80	120.83	21.91	7.62	−273.05	99.09	−22.17	109.75	−7.35

the following section, approximately 40% of the contribution of V_{ijk}^R is due to relativistic boost corrections to the NNI , and a more plausible theory is therefore obtained by removing this boost contribution from the UIX interaction.

The total energies, calculated in the manner previously described for SNM and PNM, appear in Tables VI and VII, and in Figs. 2 and 3. The pronounced kink in the $E(\rho)$ of SNM with V_{ijk}, at $\rho=0.32$ fm^{-3}, is due to the phase transition; the corresponding feature in PNM is a somewhat more subtle change in the slope of the curve at $\rho=0.2$ fm^{-3}.

It is evident from the $E(\rho)$ figures for SNM that without the V_{ijk}, the present calculation cannot explain the empirical saturation density ρ_0, of nuclear matter. As previously noted, the strength of V_{ijk}^R is adjusted to obtain the correct equilibrium density in calculations with V_{ijk}. However, the present calculations with V_{ijk} underbind SNM at saturation density, giving $E(\rho_0)\sim-12$ MeV per nucleon instead of the empirical value of ~-16 MeV. This discrepancy is presumably due to the use of imperfect variational wave functions, which do not include, for example, three- and higher-body correlations. It is known from comparison of the results of variational Monte Carlo (VMC) and exact GFMC calculations [30,31], that variational wave functions of the present form underbind the light p-shell nuclei. The variational energy of ^{8}Be for example, is above the exact GFMC result by $\sim$12%, even after incorporating into the wave function some of the three-body correlations, which we have neglected here.

In LOB calculations of Engvik *et al.* [19] the SNM energy at ρ_0 obtained from the CD-Bonn interaction model is $\sim$2 MeV lower than that obtained from A18. The difference between the results obtained with the Nijmegen models and A18 is even smaller. In order to compensate for this difference, the strength of V_{ijk}^R to be used with CD-Bonn model will have to be larger by approximately 30%, neglecting the difference between SNM wave functions predicted by the two models. An increase of this order of magnitude will also

TABLE V. Contributions of pion-exchange and phenomenological parts of nuclear interactions to the $E(\rho)$ in MeV.

	SNM		SNM				PNM		PNM			
	A18		A18+	UIX			A18		A18+	UIX		
ρ	$\langle v_{ij}^\pi\rangle$	$\langle v_{ij}^R\rangle$	$\langle v_{ij}^\pi\rangle$	$\langle v_{ij}^R\rangle$	$\langle V_{ijk}^{2\pi}\rangle$	$\langle V_{ijk}^R\rangle$	$\langle v_{ij}^\pi\rangle$	$\langle v_{ij}^R\rangle$	$\langle v_{ij}^\pi\rangle$	$\langle v_{ij}^R\rangle$	$\langle V_{ijk}^{2\pi}\rangle$	$\langle V_{ijk}^R\rangle$
0.04	−11.4	−6.4	−11.8	−6.4	−0.4	0.3	−1.7	−9.0	−1.8	−9.1	0.1	0.1
0.08	−19.2	−12.1	−19.1	−12.1	−0.8	1.5	−2.7	−16.1	−3.0	−16.3	0.3	0.8
0.12			−27.5	−16.0	−2.1	3.4			−3.9	−23.2	0.6	2.2
0.16	−32.6	−20.9	−35.3	−19.8	−3.6	6.4	−4.6	−29.3	−4.1	−29.9	1.2	4.5
0.20			−42.0	−22.8	−5.5	10.6			−17.2	−22.9	−8.7	10.1
0.24	−41.3	−28.1	−48.5	−24.6	−8.1	15.9	−5.8	−41.1	−19.1	−28.0	−10.1	15.2
0.32	−47.7	−33.7	−59.8	−27.6	−13.3	30.9	−6.3	−50.4	−25.1	−36.4	−17.4	30.6
0.40	−54.7	−36.7	−72.6	−17.4	−38.4	53.0	−7.4	−56.9	−30.1	−41.4	−24.2	50.9
0.48	−61.2	−37.6	−81.4	−16.8	−50.2	80.3	−9.6	−63.4	−35.7	−44.7	−34.1	78.0
0.56	−65.7	−37.0	−91.5	−12.0	−65.2	114.5	−33.0	−41.9	−41.6	−46.3	−47.2	112.7
0.64	−66.9	−35.8	−99.4	−7.3	−82.0	155.9	−39.2	−42.2	−52.2	−41.1	−76.9	160.3
0.80	−67.1	−40.5	−112.1	8.5	−117.7	260.2	−42.3	−34.4	−63.3	−31.2	−116.3	267.9
0.96	−70.9	−19.5	−121.2	38.0	−169.4	397.7	−46.2	−11.9	−70.9	−15.5	−155.0	402.5

TABLE VI. The $E(\rho)$ of SNM in MeV.

ρ	A18	A18+δv	A18+UIX	A18+δv+UIX*	corrected
0.04	−4.28	−4.08	−4.39	−4.31	−6.48
0.08	−8.72	−8.07	−8.06	−7.97	−12.13
0.12			−10.52	−10.54	−15.04
0.16	−14.59	−12.54	−11.85	−12.16	−16.00
0.20			−11.28	−12.21	−15.09
0.24	−17.61	−13.69	−8.99	−10.89	−12.88
0.32	−18.13	−11.87	0.84	−4.21	−5.03
0.40	−16.37	−7.70	12.23	2.42	2.13
0.48	−12.21	−1.01	32.18	15.56	15.46
0.56	−5.79	8.16	59.99	34.42	34.39
0.64	2.76	19.54	95.05	58.36	58.35
0.80	25.01	45.24	188.51	121.25	121.25
0.96	56.51	82.63	313.46	204.02	204.02

approximately bridge the difference of ~0.4 MeV between the A18 and CD-Bonn triton energies, and give give a saturation density near ρ_0 with the CD-Bonn model. These estimates are certainly very crude, since the difference between the wave functions is probably not entirely negligible. Nevertheless it is very likely that results obtained from Hamiltonians containing realistic two- and three-body forces, adjusted to reproduce the triton binding energy, the SNM density and other relevant data, will be less model dependent than those obtained with Hamiltonians containing only realistic two-body forces. The differences between the off shell behavior of the two-body forces will be partially compensated by those in the three-body forces accompanying the two-body force model.

III. RELATIVISTIC BOOST CORRECTION TO THE NN INTERACTION

In all analyses, the NN scattering data is reduced to the center of mass frame and fitted using phase shifts calculated from the NNI, v_{ij}, in that frame. The v_{ij} obtained by this procedure describes the NN interaction in the frame in which the total momentum $\mathbf{P}_{ij}=\mathbf{p}_i+\mathbf{p}_j$ is zero. In general, the interaction between particles depends upon their total momentum, and can be written as

$$v(\mathbf{P}_{ij})=v_{ij}+\delta v(\mathbf{P}_{ij}), \tag{3.1}$$

where v_{ij} is the interaction for $\mathbf{P}_{ij}=0$, and $\delta v(\mathbf{P}_{ij})$ is the boost interaction [22] which is zero when $\mathbf{P}_{ij}=0$.

It is useful to consider a familiar example. The Coulomb-Breit electromagnetic interaction [32] between two particles of mass m and charge Q, ignoring spin dependent terms for brevity, is given by

$$v(\mathbf{p}_i,\mathbf{p}_j)=\frac{Q^2}{r_{ij}}\left(1-\frac{\mathbf{p}_i\cdot\mathbf{p}_j}{2m^2}-\frac{\mathbf{p}_i\cdot\mathbf{r}_{ij}\,\mathbf{p}_j\cdot\mathbf{r}_{ij}}{2m^2r_{ij}^2}\right), \tag{3.2}$$

up to terms quadratic in the velocities of the interacting particles. In our notation it is expressed as

$$v(\mathbf{p}_i,\mathbf{p}_j)=v_{ij}+\delta v(\mathbf{P}_{ij}), \tag{3.3}$$

with

TABLE VII. The $E(\rho)$ of PNM in MeV.

ρ	A18	A18+δv	A18+UIX	A18+δv+UIX*
0.02			4.35	4.45
0.04	6.06	6.32	6.23	6.45
0.08	8.53	9.26	9.21	9.65
0.12			12.71	13.29
0.16	12.33	14.51	17.38	17.94
0.20			23.47	22.92
0.24	16.69	20.76	28.85	27.49
0.32	22.19	28.59	43.28	38.82
0.40	29.41	38.10	63.79	54.95
0.48	38.91	50.35	90.46	75.13
0.56	49.08	66.00	123.93	99.75
0.64	59.37	81.15	165.40	127.58
0.80	88.27	119.46	273.37	205.34
0.96	125.29	167.02	412.30	305.87

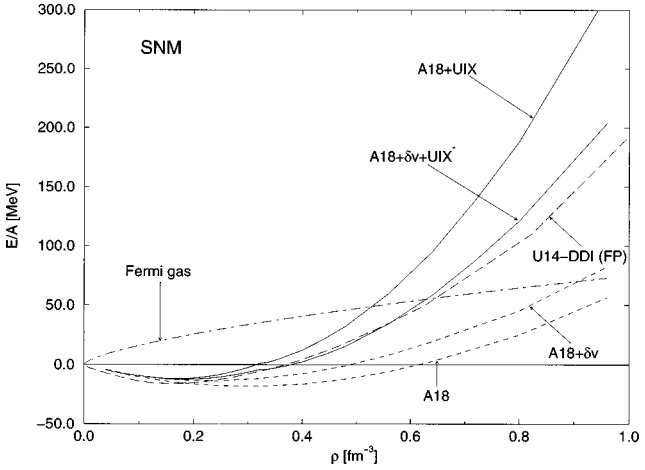

FIG. 2. The energy per nucleon, $E(\rho)$, of SNM for various interaction models.

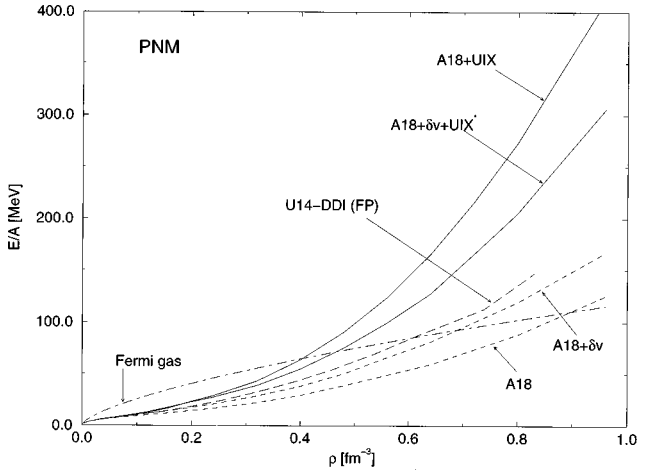

FIG. 3. The energy per nucleon, $E(\rho)$, of PNM for various interactions models.

$$v_{ij}=\frac{Q^2}{r_{ij}}\left(1+\frac{p_{ij}^2}{2m^2}+\frac{(\mathbf{p}_{ij}\cdot\mathbf{r}_{ij})^2}{2m^2r_{ij}^2}\right), \tag{3.4}$$

$$\delta v(\mathbf{P}_{ij})=-\frac{Q^2}{r_{ij}}\left(\frac{P_{ij}^2}{8m^2}+\frac{(\mathbf{P}_{ij}\cdot\mathbf{r}_{ij})^2}{8m^2r_{ij}^2}\right), \tag{3.5}$$

where $\mathbf{p}_{ij}=(\mathbf{p}_i-\mathbf{p}_j)/2$ is the relative momentum.

In all realistic models of v_{ij}, such as the A18, the dependence on $\mathbf{p}_{ij}$ is included in the momentum-dependent part of the interaction, v_{ij}^{MD}. However, we have neglected the $\delta v(\mathbf{P}_{ij})$ in the calculations presented in the previous section. Even though contributions of the boost interaction to the binding energy of SNM and ^{3}H were estimated by Coester and co-workers years ago [33,34], these contributions have been neglected in most subsequent studies of dense matter.

Following the work of Krajcik and Foldy [35], Friar [36] obtained the following equation relating the boost interaction of order P^2 to the interaction in the center of mass frame:

$$\delta v(\mathbf{P})=-\frac{P^2}{8m^2}v+\frac{1}{8m^2}[\mathbf{P}\cdot\mathbf{r}\ \mathbf{P}\cdot\nabla,v]$$
$$+\frac{1}{8m^2}[(\boldsymbol{\sigma}_i-\boldsymbol{\sigma}_j)\times\mathbf{P}\cdot\nabla,v]. \tag{3.6}$$

The general validity of this equation in relativistic mechanics and field theory was recently discussed [22]. Incorporating the boost into the interaction yields a nonrelativistic Hamiltonian of the form

$$H_{NR}^*=\sum\frac{p_i^2}{2m}+\sum(v_{ij}+\delta v(\mathbf{P}_{ij}))+\sum V_{ijk}^*+\cdots, \tag{3.7}$$

where the ellipsis denotes the three-body boost, and four and higher body interactions. This H_{NR}^* contains all terms quadratic in the particle velocities, and is therefore suitable for complete studies in the nonrelativistic limit.

Studies of light nuclei using the VMC method [37,38] find that the contribution of the two-body boost interaction to the energy is repulsive, with a magnitude which is 37% of the V_{ijk}^R contribution. The boost interaction thus accounts for a significant part of the V_{ijk}^R in Hamiltonians which fit nuclear energies neglecting δv.

In the present calculations we keep only the terms of the boost interaction associated with the static part of v_{ij}, and neglect the last term in Eq. (3.6). That term is responsible for Thomas precession and quantum contributions that are negligibly small here [39]. Our δv is given by

$$\delta v(\mathbf{P})=-\frac{P^2}{8m^2}v^s+\frac{1}{8m^2}\mathbf{P}\cdot\mathbf{r}\ \mathbf{P}\cdot\nabla v^s. \tag{3.8}$$

The two terms are due to the relativistic energy expression and Lorentz contraction, and are denoted δv^{RE} and δv^{LC}, respectively. The three-nucleon interaction used in the H_{NR}^* Eq. (3.7) is denoted by V_{ijk}^*. Its parameters are obtained by fitting the binding energies of ^{3}H and ^{4}He, and the equilibrium density of SNM, including δv. The strength of V_{ijk}^{R*} is 0.63 times that of V_{ijk}^R in UIX, while that of $V_{ijk}^{2\pi}$ is unchanged. The resulting model of V_{ijk} is called UIX*.

The approximate Hamiltonian H_{NR}, containing A18 and UIX interactions without δv, and the more correct Hamiltonian H_{NR}^*, containing A18, UIX* and δv interactions, yield very similar results for light nuclei up to ^{8}Be [38] and for SNM up to equilibrium density. However, the two models differ at higher densities, since the contributions of δv and V_{ijk}^R have different density dependences.

One may also consider relativistic nuclear Hamiltonians of the type

$$H_R=\sum\sqrt{p_i^2+m^2}+\sum(\tilde{v}_{ij}+\delta v(\mathbf{P}_{ij}))+\sum\tilde{V}_{ijk}+\cdots, \tag{3.9}$$

which require re-fitting the two-nucleon scattering data to determine the two-body interaction, $\tilde{v}_{ij}$, using relativistic kinetic energies [37]. In light nuclei, the δv contribution accounts for most of the difference between the energies obtained with H_R and H_{NR}, since the difference between the contributions of the nonrelativistic and relativistic kinetic energies is largely cancelled by the difference in interaction energy contributions from v_{ij} and $\tilde{v}_{ij}$. The results obtained with H_{NR}^* are very close to those from H_R, indicating that the former represents a significant improvement over H_{NR}.

A. Calculation of boost interaction energy

The relativistic boost contributions are calculated by evaluating terms in the cluster expansion of $\langle\delta v_{ij}^{RE}\rangle$ and $\langle\delta v_{ij}^{LC}\rangle$. In addition to the dominant two-body cluster, we have calculated dressed three-body separable diagrams and central chain diagrams.

In the case of the two-body cluster, the gradients in the center of mass momentum operator, $P_{ij}=-i(\nabla_i+\nabla_j)$, can act only on the Fermi gas part of the wave function, since the correlations f_{ij} depend only on the relative coordinate. Thus, the two-body cluster contribution to $\langle\delta v_{ij}^{RE}\rangle$ is

$$C_{2B}^{RE}(dir)=-\frac{k_F^2}{8m^2}\frac{3}{5}\rho$$
$$\times\sum_{pmp'}\int d^3r_{ij}(f^pv^mf^{p'})_{ij}C(O_{ij}^pO_{ij}^mO_{ij}^{p'}) \tag{3.10}$$

$$C_{2B}^{RE}(ex)=\frac{1}{8m^2}\frac{\rho}{s}\sum_{pmp'n}\int d^3r_{ij}(l'^2-l\nabla^2l)_{ij}$$
$$\times(f^pv^mf^{p'})_{ij}C(O_{ij}^nO_{ij}^pO_{ij}^mO_{ij}^{p'}). \tag{3.11}$$

The quantities $C(\cdots)$ in the integrand of these expressions represent the spin-isospin-independent part (or ''C-part'') of the operator product enclosed by the parentheses. Only the C-part of operator products appear in the cluster integrals, since the energy expectation value requires a sum over all possible σ_z and τ_z [6], which average to zero in isotropic

matter. In the case of SNM the indices p,m,p' run over the first six operators, as we boost only the static interactions and consider only static correlations in this calculation. The index $n=1,4$ comes from the exchange operator. In the case of PNM the $\boldsymbol{\tau}_i\cdot\boldsymbol{\tau}_j$ operators are eliminated from the Hamiltonian, thus the indices p,m,p' and n can represent only unit or spin-dependent operators. The exchange operator also contributes a factor of $1/s$, where s is the degeneracy of the system (4 for SNM, 2 for PNM).

The $C_{2B}^{RE}(dir)$ differs from the corresponding expression for the two-body direct contribution to $\langle v_{ij}^s\rangle$ by a factor $-(1/8m^2)(6k_F^2/5)$, which is the expectation value of $-P_{ij}^2/(8m^2)$ in the Fermi gas. The exchange part of the cluster, $C_{2B}^{RE}(ex)$, has the same form as the corresponding expression for $\langle v_{ij}^s\rangle_{2B}(ex)$, with l^2 replaced by $-(2/8m^2)(l'^2-l\nabla^2 l)$, where $l\equiv l(k_F r)$ is the Slater function. This expression results from gradients in P_{ij}^2 acting on the plane waves

$$\frac{1}{A\Omega}\sum_{ij} e^{-i(\mathbf{k}_i\cdot\mathbf{r}_j+\mathbf{k}_j\cdot\mathbf{r}_i)}(-\nabla_i^2-\nabla_j^2-2\nabla_i\cdot\nabla_j)e^{+i(\mathbf{k}_i\cdot\mathbf{r}_i+\mathbf{k}_j\cdot\mathbf{r}_j)}$$
$$=2\rho[(l'(k_F r_{ij}))^2-l(k_F r_{ij})\nabla^2 l(k_F r_{ij})]. \tag{3.12}$$

Here, A is the number of nucleons, Ω is the normalization volume, and since we are in the thermodynamic limit, $A/\Omega=\rho$.

The two-body cluster contribution to $\langle \delta v_{ij}^{LC}\rangle$ is

$$C_{2B}^{LC}(dir)=\frac{k_F^2}{8m^2}\frac{\rho}{5}\times\sum_{pmp'}\int d^3r_{ij}\left(f^p r\frac{dv^m}{dr}f^{p'}\right)_{ij} C(O_{ij}^p O_{ij}^m O_{ij}^{p'}) \tag{3.13}$$

$$C_{2B}^{LC}(ex)=-\frac{1}{8m^2}\frac{\rho}{s}\sum_{pmp'n}\int d^3r_{ij}(l'^2-ll'')_{ij}\times\left(f^p r\frac{dv^m}{dr}f^{p'}\right)_{ij} C(O_{ij}^n O_{ij}^p O_{ij}^m O_{ij}^{p'}), \tag{3.14}$$

which is simply the cluster contribution of a nonrelativistic potential $r\,dv/dr$, with the direct term multiplied by $(2/5)(k_F^2/8m^2)$, and with the l^2 in the exchange term replaced by $(2/8m^2)(l'^2-ll'')$. As in the δv^{RE} case, the extra factors in $\langle \delta v^{LC}\rangle$ result from the gradients in δv^{LC} acting on the Fermi gas part of the wave function.

The three-body separable diagrams represent the most significant many-body cluster contributions to the boost energy. The direct term for a boost δv^x, where $x=RE$ or LC, has the form

$$\frac{1}{A\Omega^3}\sum_{ijk}\sum_{pmp'qq'}\int d^3r_k d^3r_{ij} d^3R_{ij} e^{-i(\mathbf{k}_k\cdot\mathbf{r}_k+\mathbf{k}_{ij}\cdot\mathbf{r}_{ij}+\mathbf{K}_{ij}\cdot\mathbf{R}_{ij})} C\left(\frac{1}{4}\{f_{ij}^p O_{ij}^p, f_{ik}^q O_{ik}^q\}(\delta v_{ij}^x)^m O_{ij}^m\{f_{ij}^{p'} O_{ij}^{p'}, f_{ik}^{q'} O_{ik}^{q'}\}\right.$$
$$\left.-(f^p O^p(\delta v^x)^m f^{p'} O^{p'})_{ij}(f^q O^q f^{q'} O^{q'})_{ik}\right) e^{i(\mathbf{k}_k\cdot\mathbf{r}_k+\mathbf{k}_{ij}\cdot\mathbf{r}_{ij}+\mathbf{K}_{ij}\cdot\mathbf{R}_{ij})}. \tag{3.15}$$

The plane waves are written here in terms of the relative momentum, $\mathbf{k}_{ij}=(\mathbf{k}_i-\mathbf{k}_j)/2$, and the center of mass momentum, $\mathbf{K}_{ij}=\mathbf{k}_i+\mathbf{k}_j$, of the interacting pair. The interacting exchange $(ij-ex)$ and the passive exchange $(ik-ex)$ expressions are obtained from the above by inserting the appropriate exchange operators $[(1/s)\Sigma_{n=1,4}O_{ij}^n$ or $(1/s)\Sigma_{n=1,4}O_{ik}^n]$ to the far left of each operator product, and replacing the first plane wave product by $e^{-i(\mathbf{k}_k\cdot\mathbf{r}_k-\mathbf{k}_{ij}\cdot\mathbf{r}_{ij}+\mathbf{K}_{ij}\cdot\mathbf{R}_{ij})}$ or $e^{-i(\mathbf{k}_i\cdot\mathbf{r}_k-\mathbf{k}_{jk}\cdot\mathbf{r}_{ij}+\mathbf{K}_{jk}\cdot\mathbf{R}_{ij})}$.

Following the notation used in the calculation of the MD interaction energy [40,21], separable diagrams are classified as K-diagrams and F-diagrams. The former have gradients in δv^x acting on the Fermi gas part of the wave function, and the latter have them acting on the correlation operators F_{ik}. As with the two-body cluster contribution C_{2B}^x, the K-diagrams depend linearly on the Fermi kinetic energy. While C_{2B}^x scales as ρT_F, like the $\langle v^{MD}\rangle_{2B}$, the K-diagram contributions scale roughly as $\rho^2 T_F$. The K-diagrams generally make only small contributions to $\langle \delta v^x\rangle$, the major separable contributions coming from F-diagrams. The relatively large contribution of the F-diagrams, versus the K-diagrams, can be understood in the following way. The correlated particle k in the separable diagram modifies the center of mass momentum of the interacting pair ij via F_{ik}, thus enhancing the boost correction. As the form of the F-diagram integrals suggest, we find that their contributions exhibit the same scaling behavior as $\langle v^{MD}\rangle_{MB}$, namely as $\rho\langle T\rangle_{2B}$.

K-diagram contributions to $\langle \delta v_{ij}^{RE}\rangle$ have been evaluated for the direct three-body separable diagram and the interacting exchange diagram. These contributions factorize into an integral over r_{ij}, which is simply the corresponding two-body boost diagram, and an integral over r_{ik}. The latter integral is a so-called single-loop vertex correction, which is included in the more general vertex correction, $M_{dd}-1$, to $\langle v_{ij}^s\rangle$, defined in [6]. The direct K-diagram contribution is

$$W_s^{RE}(K,dir)=-\frac{k_F^2}{8m^2}\frac{3}{5}\rho\sum_{pmp'q}\int d^3r_{ij}(f^p v^m f^{p'})_{ij} K^{pmp'} A^{p'} A^q \frac{\rho}{2}\int d^3r_{ik}(f_{ik}^q)^2(D_{pq}+D_{mq}+D_{p'q}), \tag{3.16}$$

where the $K^{pmp'}$, A^p, and D_{pq} matrices, defined in [6], give the C-parts taking into account the non-commutativity of operators O_{ij}^p and O_{ik}^q. The corresponding interacting exchange contribution is given by

$$W_s^{RE}(K,ij-ex)=\frac{1}{8m^2}\frac{\rho}{s}\sum_{pmp'qm'n}\int d^3r_{ij}(l'^2-l\nabla^2 l)_{ij}(f^p v^m f^{p'})_{ij}\frac{1}{2}(K^{npm'}K^{mp'm'}+K^{pmm'}K^{p'nm'})A^{m'}$$
$$\times\rho\int d^3r_{ik}(f_{ik}^q)^2A^q\left(D_{qm'}+\frac{1}{2}D_{qm}+\frac{1}{2}D_{qn}\right). \tag{3.17}$$

The F-diagram contributions to $\langle \delta v_{ij}^{RE}\rangle$ are evaluated for the direct, interacting exchange and passive exchange terms. These contributions also factor into separate integrals, where the r_{ij} integral has the form of the two-body contribution to $\langle v^s\rangle$, and the r_{ik} integral is a new type of vertex correction involving gradients of the f_{ik}. The direct and ij-exchange integrals are

$$W_s^{RE}(F,dir)=\sum_{pmp'q}\frac{\rho}{2}\int d^3r_{ij}(f^p v^m f^{p'})_{ij}K^{pmp'}A^{p'}\frac{\rho}{4m^2}\int d^3r_{ik}f_{ik}^q\left(\nabla^2 f^q-\frac{6}{r^2}f^q(\delta_{q5}+\delta_{q6})\right)_{ik}$$
$$\times\left[\frac{1}{4}(D_{pq}+D_{mq}+D_{p'q})+1\right]A^q, \tag{3.18}$$

$$W_s^{RE}(F,ij-ex)=\sum_{pmp'qm'n}\left(-\frac{\rho}{2s}\right)\int d^3r_{ij}(l^2 f^p v^m f^{p'})_{ij}\frac{1}{2}(K^{npm'}K^{mp'm'}+K^{pmm'}K^{p'nm'})A^{m'}$$
$$\times\frac{\rho}{4m^2}\int d^3r_{ik}f_{ik}^q\left(\nabla^2 f^q-\frac{6}{r^2}f^q(\delta_{q5}+\delta_{q6})\right)_{ik}\left[\frac{1}{2}D_{qm'}+\frac{1}{4}D_{qm}+\frac{1}{4}D_{qn}+1\right]A^q. \tag{3.19}$$

The ik-exchange contribution is evaluated only to leading order, namely for the cases where at least one f_{ik} is a central link. In this approximation, this contribution takes the form

$$W_s^{RE}(F,ik-ex)=\sum_{pmp'n}\left(-\frac{\rho}{2}\right)\int d^3r_{ij}(f^p v^m f^{p'})_{ij}K^{pmp'}A^{p'}\frac{1}{4m^2}\frac{\rho}{s}\int d^3r_{ik}l_{ik}^2\Big[(f^c\nabla^2 f^c)_{ik}+(f^c\nabla^2 f^n)_{ik}A^n\left(1+\frac{1}{2}D_{np'}\right)$$
$$+(f^n\nabla^2 f^c)_{ik}A^n\left(1+\frac{1}{2}D_{np}\right)\Big]. \tag{3.20}$$

In this equation, the index n runs from 2 to 4 only.

The K-diagram separable three-body contributions to $\langle \delta v_{ij}^{LC}\rangle$ have the same general structure as the corresponding contributions to $\langle \delta v_{ij}^{RE}\rangle$. The direct term and the interacting exchange term have been evaluated and are presented below:

$$W_s^{LC}(K,dir)=\sum_{pmp'q}\frac{k_F^2}{8m^2}\frac{\rho}{5}\int d^3r_{ij}\left(rf^p\frac{dv^m}{dr}f^{p'}\right)_{ij}K^{pmp'}A^{p'}\frac{\rho}{2}\int d^3r_{ik}(f_{ik}^q)^2A^q(D_{pq}+D_{mq}+D_{p'q}), \tag{3.21}$$

$$W_s^{LC}(K,ij-ex)=\sum_{pmp'qm'n}-\frac{1}{8m^2}\frac{\rho}{s}\int d^3r_{ij}(l'^2-ll'')_{ij}\left(rf^p\frac{dv^m}{dr}f^{p'}\right)_{ij}\frac{1}{2}(K^{npm'}K^{mp'm'}+K^{pmm'}K^{p'nm'})A^{m'}$$
$$\times\rho\int d^3r_{ik}(f_{ik}^q)^2A^q\left(D_{qm'}+\frac{1}{2}D_{qm}+\frac{1}{2}D_{qn}\right). \tag{3.22}$$

The separable three-body F-diagrams have a more complicated structure for the δv_{ij}^{LC}. The direct diagram has the general form

$$\sum_{pmp'qq'}\frac{\rho^2}{8m^2}\int d^3r_{ij}d^3r_{ik}\left(-\frac{1}{4}\right)C[\{f_{ij}^pO_{ij}^p,f_{ik}^qO_{ik}^q\}(r_{ij}\cdot\nabla_R)(\nabla(v_{ij}^mO_{ij}^m)\cdot\nabla_R)\{f_{ij}^{p'}O_{ij}^{p'},f_{ik}^{q'}O_{ik}^{q'}\}]. \tag{3.23}$$

The integrand can be written as a sum of four terms having the gradients in δv_{ij}^{LC} acting on different parts of the correlations:

TABLE VIII. Contributions of relativistic boost interactions to the $E(\rho)$ in MeV.

	A18				A18+UIX			
	SNM		PNM		SNM		PNM	
ρ	$\langle \delta v \rangle_{2B}$	$\langle \delta v \rangle_{MB}$	$\langle \delta v \rangle_{2B}$	$\langle \delta v \rangle_{MB}$	$\langle \delta v \rangle_{2B}$	$\langle \delta v \rangle_{MB}$	$\langle \delta v \rangle_{2B}$	$\langle \delta v \rangle_{MB}$
0.02							0.08	0.03
0.04	0.15	0.05	0.21	0.05	0.15	0.05	0.21	0.05
0.08	0.45	0.20	0.59	0.14	0.44	0.20	0.58	0.15
0.12					0.85	0.40	1.10	0.29
0.16	1.32	0.74	1.71	0.46	1.33	0.73	1.72	0.49
0.20					1.88	1.09	2.60	0.58
0.24	2.42	1.50	3.16	0.91	2.49	1.50	3.42	0.84
0.32	3.76	2.49	4.92	1.48	3.86	2.51	5.46	1.41
0.40	5.18	3.49	6.64	2.06	6.04	3.75	7.73	2.25
0.48	6.69	4.52	8.67	2.77	7.92	5.17	10.34	3.20
0.56	8.35	5.59	12.28	4.64	9.96	6.81	13.27	4.23
0.64	10.16	6.62	15.81	5.97	12.29	8.69	16.69	4.81
0.80	12.61	7.62	22.12	9.07	17.12	11.90	23.83	7.25
0.96	16.95	9.17	29.62	12.11	23.11	14.61	31.91	10.59

$$
\begin{aligned}
&-\frac{1}{4}\left(r f^p \frac{dv^m}{dr} f^{p'} \right)_{ij} f^q_{ik} \left(\left[(f^{q'})'' - \frac{1}{r}(f^{q'})' \right] \cos^2\theta_i + \frac{1}{r}(f^{q'})' \right)_{ik} C[\{O^p_{ij}, O^q_{ik}\} O^m_{ij} \{O^{p'}_{ij}, O^{q'}_{ik}\}] \\
&-\frac{1}{2}\left(f^p \frac{dv^m}{dr} f^{p'} \right)_{ij} (f^q (f^{q'})')_{ik} \cos\theta_i C[\{O^p_{ij}, O^q_{ik}\} O^m_{ij} \{O^{p'}_{ij}, r_{ij}\cdot\nabla O^{q'}_{ik}\}] \\
&-\frac{1}{4}\left(f^p \frac{1}{r}\frac{dv^m}{dr} f^{p'} \right)_{ij} (f^q f^{q'})_{ik} C[\{O^p_{ij}, O^q_{ik}\} O^m_{ij} \{O^{p'}_{ij}, (r_{ij}\cdot\nabla) r_{ij}\cdot\nabla O^{q'}_{ik}\}] \\
&-\frac{1}{4}(f^p v^m f^{p'})_{ij} f^q_{ik} C[\{O^p_{ij}, O^q_{ik}\} (r_{ij}\cdot\nabla_R)\nabla_R \cdot (f^{q'}_{ik} \nabla O^m_{ij} \{O^{p'}_{ij}, O^{q'}_{ik}\})].
\end{aligned} \tag{3.24}
$$

The C-parts in the above expressions depend on the cosine of the azimuthal angle, θ_i, and therefore cannot be expressed exclusively in terms of the D_{pq} matrices, which include an implicit average over that angle. The C-parts must then be individually evaluated for each operator product.

The contribution of the direct diagram is dominated by the first term in the above sum. In evaluating the interacting exchange and passive exchange diagrams, only the term corresponding to that dominant part has been included. For example, the interacting exchange contribution is approximated by

$$
\begin{aligned}
W^{LC}_s(F, ij-ex) = \sum_{pmp'qq'n} \frac{1}{8m^2}\frac{\rho^2}{s} \int d^3 r_{ij} d^3 r_{ik} \left(l^2 f^p \frac{dv^m}{dr} f^{p'} r \right)_{ij} f^q_{ik} \left(\left[(f^{q'})'' - \frac{1}{r}(f^{q'})' \right] \cos^2\theta_i + \frac{1}{r}(f^{q'})' \right)_{ik} \\
\times \frac{1}{4} C[O^n_{ij}\{O^p_{ij}, O^q_{ik}\} O^m_{ij} \{O^{p'}_{ij}, O^{q'}_{ik}\}].
\end{aligned} \tag{3.25}
$$

The corresponding passive exchange contribution was calculated with the additional simplification of considering only leading term contributions, having at least one central f^c_{ik} link.

We have also evaluated central-chain diagram contributions, denoted by W_{cch}, to the boost interaction expectation values. These diagrams are obtained by dressing two-body cluster diagrams with hypernetted central chains. Their contribution was found to be significantly smaller than the contribution from separable three-body terms.

The combined results for the two-body clusters and for the many-body clusters appear in Table VIII. The first four columns contain the boost contributions to the energy of SNM and PNM, calculated using the optimal wave functions for the A18 interaction alone, while the next four columns contain the corresponding boost contributions, calculated with the optimal wave functions for the A18+UIX. As expected, the many-body contributions to the boost interaction energy are comparable to the two-body contributions, because T_F and $\langle T \rangle_{2B}$ have similar magnitudes.

Detailed breakdowns of the boost contributions in the A18+UIX* model are presented in Tables IX and X for

TABLE IX. A18+UIX*: Contributions to $\langle \delta v^{RE} \rangle$ in MeV.

	SNM				PNM			
ρ	C_{2B}	$W_s(K)$	$W_s(F)$	W_{cch}	C_{2B}	$W_s(K)$	$W_s(F)$	W_{cch}
0.02					0.04	0.00	0.02	0.00
0.04	0.09	0.00	0.04	0.00	0.11	0.00	0.04	0.00
0.08	0.24	−0.02	0.15	0.00	0.31	−0.01	0.12	0.00
0.12	0.46	−0.04	0.31	0.00	0.58	−0.03	0.23	0.00
0.16	0.73	−0.06	0.54	0.00	0.93	−0.03	0.39	−0.01
0.20	1.03	−0.09	0.81	0.00	1.32	−0.16	0.50	−0.03
0.24	1.36	−0.14	1.11	0.00	1.73	−0.19	0.68	−0.03
0.32	2.11	−0.22	1.85	0.00	2.77	−0.32	1.14	−0.06
0.40	3.25	−0.70	3.17	−0.04	3.90	−0.40	1.69	−0.08
0.48	4.26	−0.94	4.35	−0.04	5.23	−0.51	2.34	−0.09
0.56	5.36	−1.15	5.61	−0.05	6.71	−0.66	3.05	−0.14
0.64	6.63	−1.53	7.20	−0.05	8.51	−1.00	3.68	−0.24
0.80	9.02	−1.96	9.58	−0.05	12.14	−1.43	5.41	−0.32
0.96	12.44	−3.58	13.37	−0.16	16.23	−1.87	7.65	−0.40

δv^{RE} and δv^{LC}. In all cases the bulk of the contributions come from the direct terms. Since we can integrate $\langle \delta v^{LC} \rangle$ by parts to obtain $\langle \delta v^{RE} \rangle$ plus additional terms, their expectation values should be similar in magnitude. The ratio of the contributions of δv^{LC} and δv^{RE} in SNM is found to be ~ 0.7 at all densities, while in PNM it is ~ 0.75 at $\rho < 0.2$ fm^{-3}, and $\simeq 1$ at higher densities. Results of VMC calculations [37] have shown that this ratio is ~ 0.5 in ^{3}H and ^{4}He.

The δv^{RE} has two factors, $P^2/8m^2$ and v^s, suggesting the approximation

$$\langle \delta v^{RE} \rangle \approx -\left\langle \frac{P^2}{8m^2} \right\rangle \langle v^s \rangle, \\ = -\frac{1}{2m} \langle T \rangle \langle v^s \rangle. \tag{3.26}$$

Our results show that this approximation has errors of only $\sim 10\%$ in SNM, but can be wrong by $\sim 50\%$ in PNM. Nevertheless it may be used to estimate the order of magnitude of the contribution of relativistic boost interactions.

B. Nucleon matter energies

We evaluate the boost interaction contributions as a first order perturbation. Thus the energies of nucleon matter with the A18+ δv interactions are obtained by simply adding the δv contributions listed in Table VIII to the A18 energies. The results are listed in Tables VI and VII, and shown in Figs. 2 and 3.

The three-body interaction, UIX*, to be used with A18 + δv, contains the term V_{ijk}^{R*} that is 0.63 times the V_{ijk}^{R} in the UIX. Since the boost effects are treated only in first order, the energies for the A18+ δv + UIX* interaction are obtained by adding $\langle [\delta v_{ij} - 0.37\ V_{ijk}^{R}] \rangle$ to the energies for A18+UIX interactions. The results are listed in Tables VI

TABLE X. A18+UIX*: Contributions to $\langle \delta v^{LC} \rangle$ in MeV.

	SNM				PNM			
ρ	C_{2B}	$W_s(K)$	$W_s(F)$	W_{cch}	C_{2B}	$W_s(K)$	$W_s(F)$	W_{cch}
0.02					0.03	0.00	0.01	0.00
0.04	0.07	0.00	0.02	0.00	0.09	0.00	0.03	0.00
0.08	0.20	−0.02	0.08	0.00	0.27	−0.01	0.06	0.00
0.12	0.39	−0.04	0.17	0.00	0.51	−0.01	0.11	−0.01
0.16	0.59	−0.06	0.32	−0.01	0.80	−0.02	0.18	−0.02
0.20	0.85	−0.07	0.48	−0.02	1.28	−0.12	0.42	−0.03
0.24	1.13	−0.11	0.65	−0.03	1.69	−0.13	0.55	−0.04
0.32	1.76	−0.16	1.09	−0.06	2.68	−0.20	0.92	−0.07
0.40	2.79	−0.52	1.96	−0.14	3.82	−0.23	1.37	−0.11
0.48	3.66	−0.64	2.67	−0.23	5.11	−0.29	1.93	−0.16
0.56	4.60	−0.72	3.45	−0.31	6.55	−0.37	2.55	−0.21
0.64	5.66	−0.89	4.39	−0.43	8.17	−0.59	3.19	−0.25
0.80	7.79	−0.96	5.77	−0.78	11.69	−0.85	4.81	−0.37
0.96	10.67	−1.49	7.80	−1.34	15.68	−1.06	6.82	−0.55

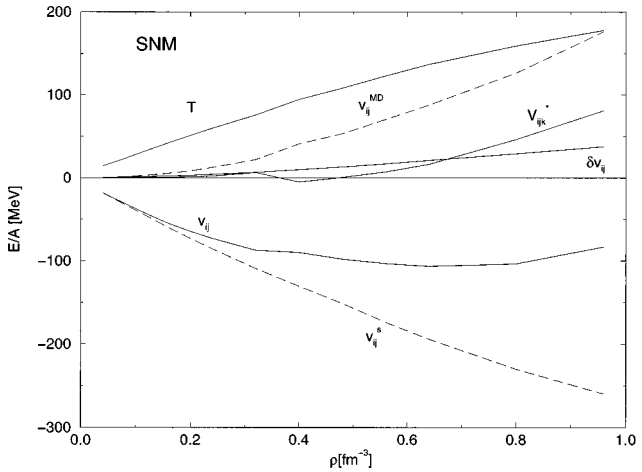

FIG. 4. Kinetic and interaction energies in A18+ δv +UIX* model of SNM.

and VII, and shown in Figs. 2 and 3. At low densities the A18+UIX and A18+ δv +UIX* interactions yield similar results. However the energies predicted by the latter model are lower than those of the former at higher densities, where $0.37\langle V^R\rangle$ is much larger than $\langle \delta v\rangle$. The difference between the energies predicted by A18+ δv and A18+ δv +UIX* interactions at higher densities is due to three-body forces; it is smaller than that between the energies obtained from A18 and A18+UIX by almost a factor of two.

The results obtained with the Urbana density-dependent interaction (U14-DDI) [10] are also shown in Figs. 2 and 3 for comparison. Since Skyrme-type interactions based on the U14-DDI $E(\rho)$ explain nuclear binding energies quite accurately, it is likely to provide a reliable representation of phenomena at $\rho \leqslant \rho_0$.

The variation of the kinetic and interaction energies with nucleon density in our most realistic model, with A18+ δv +UIX*, interactions is shown in Figs. 4 and 5. Due to a large cancellation between the contributions of $V^{2\pi}$ and V^{R*}, the total V_{ijk} contribution is now smaller than that of v_{ij}, and the δv contribution is also small. An order of magnitude estimate of the boost correction to the three body interaction is given by $\langle T\rangle\langle V_{ijk}\rangle/3m$, using generalizations

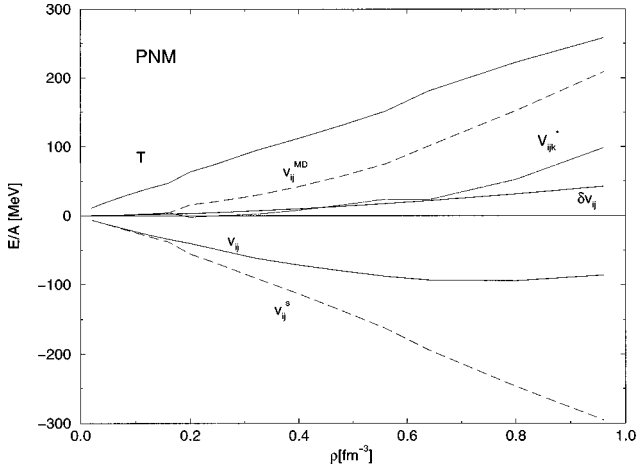

FIG. 5. Kinetic and interaction energies in A18+ δv +UIX* model of PNM.

of Eq. (3.26). This estimate is less than 10 MeV at the highest density considered. The phase equilibria are calculated after adding the boost interaction contribution, calculated in first order, separately for the phases with and without pion condensation. However, Figs. 4 and 5 show that the δv contribution is very small, and has a smooth density dependence in the region of the phase transition. Therefore the boost interactions do not have a noticeable effect on the transition density.

The most significant remaining problem appears to be our neglect of the boost corrections to the v^{MD}, the unboosted contribution of which is quite large at high densities. Such corrections involve terms of order (velocity)^4, which are beyond the scope of the present work. The kinetic energy also has corrections of that order, which we cannot include because the A18 interaction is fitted to data using nonrelativistic kinetic energy. However, the correction to the Fermi gas kinetic energy is $3k_F^4/56m^3$, which is less than 10 MeV in PNM at the density of $6\rho_0$.

The Dirac-Brueckner approximation provides another way to estimate relativistic effects using realistic models of nuclear forces. The energies of our A18+ δv +UIX* model are lower than those of lowest order Dirac-Bruekner calculations with the Bonn A potential [41]. For example, at $4\rho_0$ we obtain 58 and 128 MeV per nucleon while the Dirac-Bruekner calculation gives 76 and 164 MeV per nucleon, for SNM and PNM, respectively. However, the difference between the results of the two methods is significantly smaller than that between either of the two and the uncorrected A18 energies of 3 and 59 MeV per nucleon (Tables VI and VII).

In the last column of Table VI we list SNM energies obtained by adding a correction $\gamma_2\rho^2 e^{-\gamma_3\rho}$ to the A18+ δv +UIX* results. The empirical binding energy and density of SNM are reproduced with $\gamma_2 = 2822$ MeV fm^6, and $\gamma_3 = 18.34$ fm^3. This correction has a maximum value of 4.5 MeV at 0.11 fm^{-3}, and the ''corrected'' $E(\rho)$ of SNM is a better representation of known nuclear properties at lower densities, and is useful to obtain a smooth connection with the EOS of crustal matter. It becomes identical to the $E(\rho)$ obtained using the A18+ δv +UIX* model at higher densities.

IV. COLD CATALYZED NUCLEON MATTER

In this section we use the results of the earlier sections to calculate the equation of state and composition of cold, catalyzed matter, i.e., matter at zero temperature in its lowest energy state. Here the matter is assumed to be made up of neutrons, protons, and leptons; the possible admixture of quark matter is considered later. Since the boost interaction is clearly an integral part of the two-nucleon interaction, we regard the models A18+ δv and A18+ δv +UIX* as realistic, and discuss their results in detail. The difference between the two models demonstrates the effect of the three-nucleon interaction. Some of the results obtained with the less realistic models without the boost interaction are also presented for comparison.

Matter at zero pressure, at the surface of a neutron star, is made up of atoms of ^{56}Fe, just as in terrestrial iron. This is the most stable form of electrically neutral matter composed of neutrons, protons, and electrons. Below the neutron star

surface, as a result of the increased pressure of the matter caused by the gravitational attraction, the atoms become completely ionized and the electrons form a relativistic Fermi gas, whose Fermi energy becomes competitive in magnitude with nuclear energies [42]. Consequently, electron capture by the protons can occur. As a result, with increasing depth below the stellar surface the nuclei become more neutron rich, and cross the neutron-drip line. At this point the most energetic neutron orbitals have become unbound, and the matter consists of neutron-rich nuclei immersed in a neutron gas, whose density also increases as the pressure is increased further. The baryon number density at which this transition occurs is about 2×10^{-4} fm^{-3}. As the pressure and density continue to increase, the charge number Z of the nuclei remains in the range $30-40$ but the mass number A grows steadily, and the distance between nuclei decreases. In the density range above about 0.06 fm^{-3}, where the volumes occupied by nuclei and by the surrounding neutron gas become comparable, the matter may undergo an inversion to bubbles of neutron gas surrounded by nuclear matter by going through a progression of phases involving nonspherical shapes, although this aspect of the crustal structure is somewhat model dependent [11,43]. At a density above about 0.1 fm^{-3} there no longer occur nuclei or other clumps of proton-containing matter, and cold, catalyzed matter becomes a uniform fluid of neutrons with a small fraction of protons.

A reliable discussion of the properties of matter over the crustal density range requires a nuclear model that can describe inhomogeneous matter in the geometries occurring there. The difficulties encountered cause the model dependence mentioned. However, for neutron stars with masses $\gtrsim1.4M_{\odot}$, the mass fraction contained in the crust of the star is less than about 2%. We have therefore used results of earlier work [11,43] for matter at densities $\leqslant0.1$ fm^{-3}. Since over that density range our present matter energies agree well with ones used earlier, this substitution causes negligible inconsistency in our conclusions about the total mass of the neutron star.

At densities of 0.1 fm^{-3} and greater, we require properties of charge neutral uniform matter made up of neutrons, protons, electrons and muons in beta equilibrium. At a given baryon number density $\rho=\rho_n+\rho_p$, the conditions to be satisfied by the components are charge neutrality,

$$\rho_p=\rho_e+\rho_\mu, \tag{4.1}$$

and beta equilibrium,

$$\mu_n=\mu_p+\mu_e, \quad \mu_\mu=\mu_e. \tag{4.2}$$

Here ρ_i is the number density of the species indicated by the subscript i, and μ_i is its chemical potential including rest mass. After achieving a solution to these conditions, one obtains the total pressure

$$P=P_N+P_e+P_\mu, \tag{4.3}$$

and total energy density

$$\varepsilon=\varepsilon_N+\varepsilon_e+\varepsilon_\mu, \tag{4.4}$$

of the matter, and thereby the EOS, in the form $P=P(\tilde{\rho})$, where $\tilde{\rho}=\varepsilon/c^2$ is the mass-energy density of the matter. The composition and other thermodynamic variables are also determined in this process.

The baryonic part of the matter consists of strongly interacting neutrons and protons with a given proton fraction $x_p=\rho_p/\rho$. The minimum processing necessary in order to obtain an EOS for any of the sets of SNM and PNM energies of earlier sections is to fit the energies to a smooth function of density, so that the derivatives needed to obtain chemical potentials ($\mu_i=\partial\varepsilon/\partial\rho_i$) and pressure ($P=\Sigma_i\rho_i\mu_i-\varepsilon$) can be calculated. One then needs to interpolate between the $x_p=0.5$ SNM and $x_p=0$ PNM results in order to find the value of x_p required by beta equilibrium.

The fitting procedure used earlier [44], and which we employ here, introduces more than the minimum processing just described. It uses a generalized Skyrme interaction containing a momentum and density-dependent delta function interaction. By a well-known procedure [45], the matrix elements of this interaction can be written as an energy-density functional in the form

$$H_{eff}=\left(\frac{\hbar^2}{2m}+f(\rho,x_p)\right)\tau_p+\left(\frac{\hbar^2}{2m}+f(\rho,1-x_p)\right)\tau_n + g(\rho,x_p)+H_{gradient}. \tag{4.5}$$

The number and kinetic densities $\rho_{n(p)}$ and $\tau_{n(p)}$ are defined in terms of the neutron or proton orbitals $\phi_{\alpha,n(p)}(\mathbf{r})$ by $\rho_i(\mathbf{r})=\Sigma_\alpha n_i(\alpha,T)|\phi_{\alpha,i}(\mathbf{r})|^2$ and $\tau_i(\mathbf{r})=\Sigma_\alpha n_i(\alpha,T)|\nabla\phi_{\alpha,i}(\mathbf{r})|^2$, where the Fermi-statistics density of states $n_i(\alpha,T)=[1+\exp((e_{\alpha,i}-\mu_i)/T)]^{-1}$ at $T=0$ become a step function $\Theta(e_{\alpha,i}-\mu_i)$. The function f in Eq. (4.5) comes from the assumed momentum dependence of the interaction, and is parametrized in the form

$$f(\rho,x_p)=f_0(\rho)+x_pf_1(\rho). \tag{4.6}$$

It produces density- and isospin-dependent effective nucleon masses $m_i^*(\rho,x_p)$,

$$\frac{\hbar^2}{2m_p^*(\rho,x_p)}=\frac{\hbar^2}{2m}+f(\rho,x_p),$$

$$\frac{\hbar^2}{2m_n^*(\rho,x_p)}=\frac{\hbar^2}{2m}+f(\rho,1-x_p). \tag{4.7}$$

The term $H_{gradient}$ in Eq. (4.5) depends on gradients of the densities, and thus affects finite systems; it is determined uniquely by the functions f [43]. The relation between τ_i and ρ_i depends on temperature via the Fermi functions. Therefore knowledge of the matter energies at finite temperatures, as was given in Ref. [10], permits a determination of $f(\rho,x_p=0.5)$ and $f(\rho,x_p=0)$, i.e., $f_0(\rho)$ and $f_1(\rho)$ in Eq. (4.6). The potential-energy terms $g(\rho,x_p=0.5)$ and $g(\rho,x_p=0)$ may then be obtained by comparison with the zero-temperature energies. The functional forms used for $f(\rho,x_p=0.5,0)$ and $g(\rho,x_p=0.5,0)$ are chosen to represent with appropriate accuracy the calculated energies; it is not sufficient, nor necessary, that they have the extremely simple

power dependence on ρ of customary Skyrme interactions. The effective interaction FPS obtained in this manner from the SNM and PNM energies calculated with the U14-DDI interaction has been described and used elsewhere [44,43,11].

In the present work, we have studied the matter energies only at zero temperature, and cannot therefore make a new determination of the momentum-dependent (τ-containing) terms in H_{eff}. Rather than omitting them, we have kept intact the τ-dependent terms from the earlier determination [44], and have modified only the potential energy term $g(\rho,x_p)$. To facilitate handling of the two different phases, we make separate fits to the normal low density phase (LDP) and the high density phase (HDP) with pion condensation. The analytic forms used for the fitting are given in Appendix A. They are chosen solely to provide an economical fit to the calculated energies.

The interpolation between $x_p=0.5$ and $x_p=0$ is carried out assuming a $(1-2x_p)^2$ dependence of the energy at a given density. It is well known that matter energies, as a function of x_p, can be expanded in powers of $(1-2x_p)$ about $x_p=0.5$. Previous studies [46], using cluster expansion techniques [6], have found that the quartic terms are small, and that the quadratic terms determined from results at $x_p=0$ and 0.5 are sufficient to obtain few percent accuracy in the interpolation. The potential energy terms g in the effective interaction Eq. (4.5) obtained by fitting to PNM and SNM are therefore interpolated by means of the expression

$$g(\rho,x_p)=g(\rho,x_p=0.5)(1-(1-2x_p)^2) + g(\rho,x_p=0)(1-2x_p)^2. \tag{4.8}$$

A. The phase transition

In fitting the results of the calculations described in Secs. I–III, we find that the SNM and PNM energies coming from the models that include a three-nucleon interaction have a clear discontinuity in slope, associated with the phase transition, so that different analytic forms are needed above and below the critical densities, $\rho_t=0.20$ fm^{-3} for PNM, 0.32 fm^{-3} for SNM. In Fig. 6 the energies and the fits are shown for the A18+ δv + UIX* model. (Here, and for the rest of the paper, we use for the SNM energies of this model the ''corrected'' values given in the last column of Table VI.) The A18+ δv and A18 models do not show such a discontinuity in any marked way.

An important assumption of our treatment of the two phases of nuclear matter and the phase transition, as exhibited in Fig. 6, is that the analytic forms fitted to the PNM and SNM energies of each phase may be extrapolated beyond the density region in which they are determined. Since the equilibrium is a two-dimensional phenomenon, the energy as a function of ρ and x_p can be represented by a surface above the ρ,x_p plane. The interpolation described in the last subsection makes the energy surface of the LDP a valley parabolic in the x_p dimension extending from $x_p=0$ to $x_p=1$, with its minimum at $x_p=0.5$. A similar interpolation between the energies of the HDP produces another parabola. Note that because of the charge symmetry breaking terms in the A18 interaction only the $x_p \leqslant 0.5$ side of the parabolas is useful, and that the parabolic shape approximation has been tested only in the LDP [46].

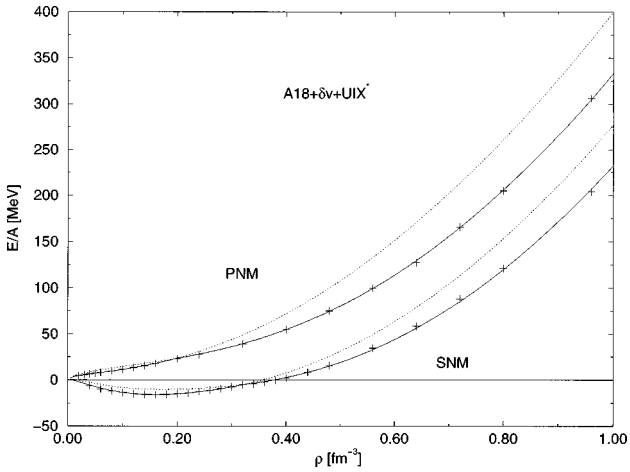

FIG. 6. The PNM and SNM energies for the A18+ δv + UIX* model, and the fits to them using an effective interaction. The full lines represent the stable phases, and the dotted lines are their extrapolations.

A transition to a neutral pion condensed phase of PNM was obtained earlier with the older Argonne v_{14} (A14) NNI and Urbana VII (UVII) TNI interactions by WFF [12]. However, with those interactions SNM has a normal ground state. WFF estimated the properties of the A14+UVII model of cold catalyzed matter by interpolating between the normal SNM and the pion condensed PNM. For the A18+ δv + UIX* interaction, we find that such a procedure overestimates the symmetry energy of the HDP by $\sim$10 to 20% in the density range 0.2 to 0.5 fm^{-3}. Fortunately we see the transition for both PNM and SNM, and can avoid that problem.

In Fig. 7 we show for the A18+ δv + UIX* model the density at which the LDP and HDP $E(\rho,x_p)$ surfaces intersect, i.e., where the interpolated phases have the same energy. The curve obtained is not necessarily a parabola in x_p,

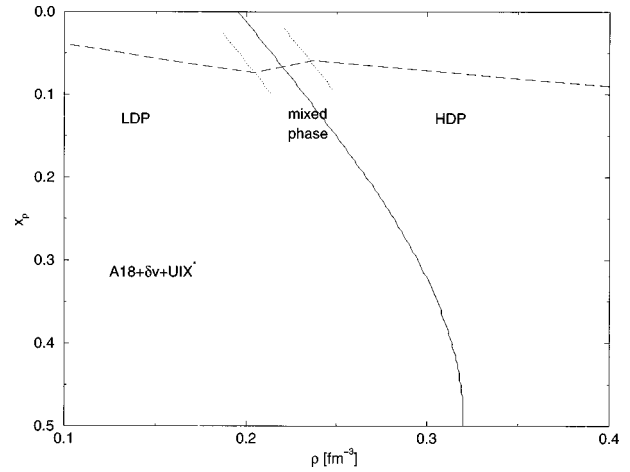

FIG. 7. On a plot of proton fraction x_p vs baryon density, for the A18+ δv + UIX* model, the boundary between the LDP and HDP, obtained in the manner described in the text. The dashed curve is the proton fraction of beta-stable matter, and the dotted lines mark the boundary of the mixed phase region.

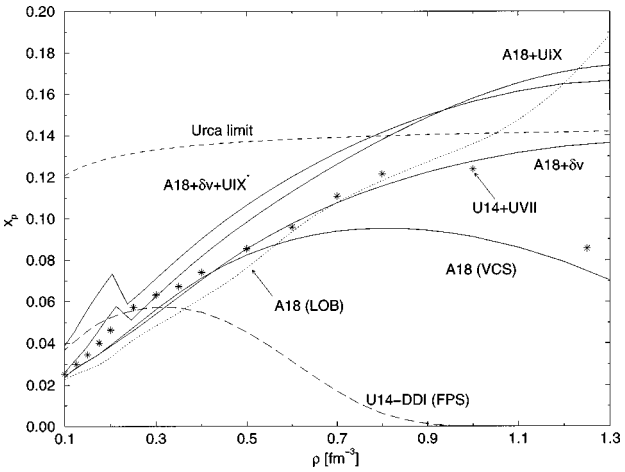

FIG. 8. For beta-stable matter, the proton fractions x_p for the four models discussed in the text vs baryon density. The dashed curve, U14-DDI (FPS), is from [11], the dotted line, A18(LOB) is from [19], the points are from [12,50] for the U14+UVII model, and the dotted line is the threshold for the direct Urca cooling process, as a function of ρ.

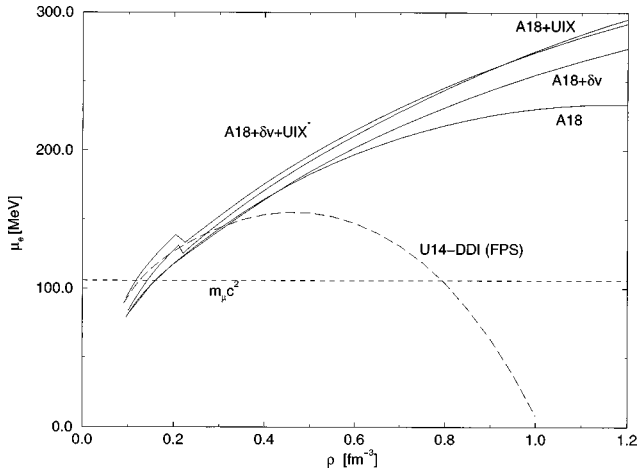

FIG. 9. For beta-stable matter, the electron chemical potentials μ_e for the four models discussed in the text vs baryon density. The dashed curve, U14-DDI (FPS), is from [11], and the horizontal line, at $\mu_e = m_\mu c^2$, is the threshold for a muon contribution to the lepton fraction.

since the density dependence of the curvature of the parabolas is more complicated than quadratic. Also shown is the proton fraction of beta-stable matter in each phase.

The transition of matter from the LDP to the HDP probably occurs via a mixed phase region in which each phase need not be charge neutral [23], as discussed in the following section. Here, for simplicity, we assume that each phase is a charge-neutral fluid and make a Maxwell construction to obtain the change in density due to the phase transition. The baryon chemical potentials, which for beta equilibrium are equal to the neutron chemical potentials, and total pressures of the two phases are equated to obtain the densities and proton fractions of the LDP and HDP in equilibrium. They are (0.204 fm^{-3},0.073) and (0.237 fm^{-3},0.057) respectively. In the region between these two densities the most stable form of the matter is a mixture of the two phases.

B. Proton fraction and μ_e

The proton fraction and the related electron chemical potential of the matter are important in assessing the cooling rates of neutron stars [47] and the possibility of kaon condensation in neutron star interiors [48,49]. For the models discussed here we plot in Fig. 8 the proton fraction x_p against baryon density. This figure also shows, for comparison, results obtained for other models and by other methods: the U14+UVII model, a predecessor of the present A18 +UIX model, as given by WFF with the VCS method; the A18 model, results of Engvik *et al.* [19] with lowest order Brueckner (LOB) calculations; the U14-DDI model [10] using the FPS effective interaction [11]. Indicated on the plot is the critical value of x_p, as a function of ρ, for the onset of the direct Urca cooling process in the presence of both electrons and muons. That process allows energy to be conducted from the interior of the star by neutrinos generated in binary thermal collisions, a very efficient process [47]. In the models containing three-nucleon interactions, the discontinuity in x_p at $\rho \sim 0.2$ fm^{-3} signals the onset of the HDP. The corresponding electron chemical potentials are plotted in Fig. 9.

As suggested in Ref. [12], the determining quantity for x_p is the symmetry energy, given approximately by $E_{sym} \approx E_{PNM} - E_{SNM}$. The LOB and VCS methods yield similar values for x_p with the A18 interaction up to $\rho = 0.6$ fm^{-3}. Beyond this density the x_p obtained from VCS calculations starts to decrease, while that from LOB calculations continues to increase with density. The VCS and LOB energies for the A18 model are compared in Fig. 10. They are not too different for PNM. For SNM, however, at $\rho > 0.6$ fm^{-3} the LOB energy is much lower than that of the VCS. The VCS E_{sym} saturates for the A18 model at $\rho \sim 0.6$ fm^{-3}, while that of LOB calculations continues to increase with density, causing the x_p to do the same. It will be interesting to see if three hole-line and higher terms [7,51] neglected in the LOB calculations reduce the difference between LOB and VCS energies.

Engvik *et al.* [19] have calculated x_p in cold matter using the LOB method with all five modern NN potentials that provide high precision fits to the Nijmegen NN scattering

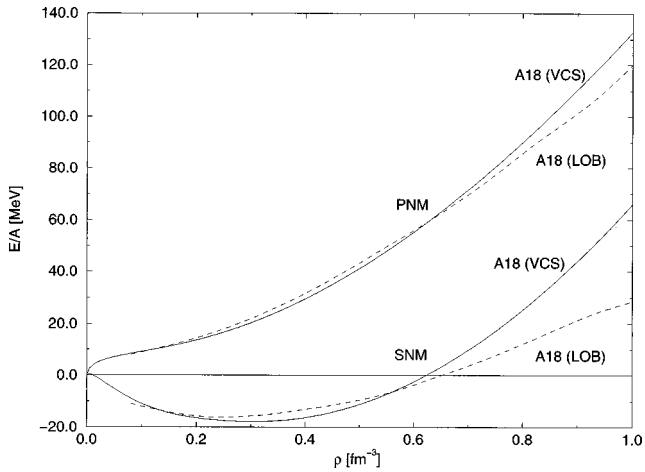

FIG. 10. Comparison of the energies of PNM and SNM obtained for the A18 model with the VCS method in the present work, and with LOB calculations by Engvik *et al.* [19].

data base. At a density of one nucleon per fm^3 the CD-Bonn model [17] gives the largest x_p of 0.15, while the Nijmegen I model [15] gives the smallest value of 0.10. The spread in these values is comparable with the difference between VCS and LOB results for A18 of $x_p = 0.09$ and 0.14 at this density.

The δv term and the three-nucleon interaction increase the symmetry energy, and push the x_p barely above the Urca limit at high densities. For the A18+ δv + UIX* model the threshold is at a density of $\rho = 0.78$ fm^{-3}, and, as discussed in the next section, stars must have a mass $> 2.0 M_\odot$ to achieve such a density. However, this density is at the limit of our calculations and of the input physics. For example, admixtures of quark matter with hadronic matter, considered in the next section, may affect the Urca process in matter at such densities.

The U14-DDI (FPS) model predicts values for x_p that are much smaller than those predicted by all other models considered here, and in fact go to zero for $\rho \sim 1$ fm^{-3}. It is based on the U14 NN interaction, also used in the U14 +UVII model. However, instead of adding the UVII three nucleon interaction to obtain the empirical saturation density of nuclear matter, it uses a density dependent modification (U14-DDI) of the U14 NN interaction [9] chosen to reproduce the energy, density and compressibility of equilibrium nuclear matter. Unlike the UVII interaction, this modification reduces the symmetry energy, and thus the x_p, at high density. The main advantage of using three-nucleon interactions, instead of density dependent modifications of the two-nucleon interaction, is that the former can be tested via accurate calculations of the light nuclei. Unfortunately, the available results [30] indicate that the UIX model may be overestimating the repulsion between three neutrons, thus overestimating the x_p; an improved version of the UIX model is currently being developed.

V. NEUTRON STARS

Using the methods just described we obtain for each model the EOS for cold, catalyzed beta-stable matter. At a baryon number density of 0.1 fm^{-3} they are joined onto an earlier EOS in which properties of the crust material has been treated more accurately [11]. The Oppenheimer-Volkoff general relativistic equations for a spherically symmetric (nonrotating) neutron star [1] are

$$\frac{dP}{dr} = -\frac{(\tilde{\rho} + P/c^2)G(m(r) + 4\pi r^3 P/c^2)\Lambda(r)}{r^2},$$

$$m(r) = \int_0^r 4\pi r^2 \tilde{\rho} dr, \tag{5.1}$$

where $\Lambda(r) = [1 - 2Gm(r)/rc^2]^{-1}$. The corresponding equations for obtaining the moment of inertia, for a slowly rotating star, are given in Appendix B. Starting from some central mass-energy density $\tilde{\rho}_c$, or equivalently from a central number density ρ_c, these equations are integrated outwards to a radius $r = R$, at which P is zero, thus yielding the stellar radius, R, the gravitational mass of the star, $M = m(R)$, and the moment of inertia I.

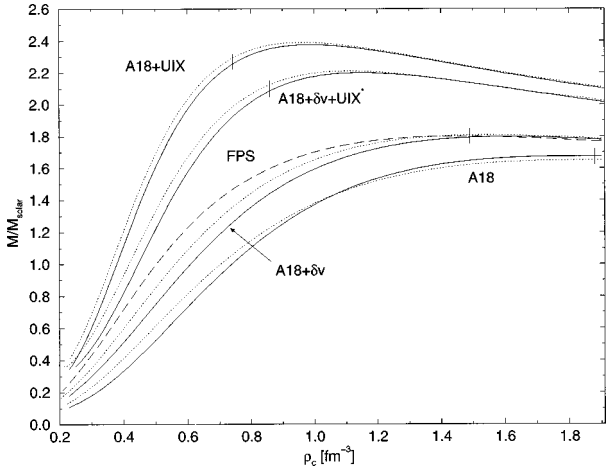

FIG. 11. Neutron star gravitational mass, in solar masses, vs central baryon density, for the four models described in the text. The full curves are for beta-stable matter, and the dotted lines are for pure neutron matter. The vertical lines show the density above which the matter is superluminal. The dashed curve, FPS, is from [11].

The dependence of the neutron star mass on central baryon density ρ_c for the four models is shown in Fig. 11. In order to estimate the effect of beta-stability on these results, we show also the trajectories obtained by using the pure neutron matter EOS for densities greater than 0.1 fm^{-3}, joined to the crust results of Ref. [11]. Earlier results with the FPS EOS [11] are included for comparison. For the same set of results, the neutron star mass is plotted against the star radius in Fig. 12.

The maximum masses for the five models illustrated in Figs. 11 and 12 are listed in Table XI. While the models based on only two-nucleon interactions have maximum masses at or below $1.8 M_\odot$, those for the two models containing three-nucleon interactions have maximum masses well above $2 M_\odot$. The model that we believe includes most of the necessary physics is A18+ δv + UIX*, which yields a maximum mass of $2.2 M_\odot$. This model achieves its maximum mass for a central baryon density $\rho_c = 1.14$ fm^{-3},

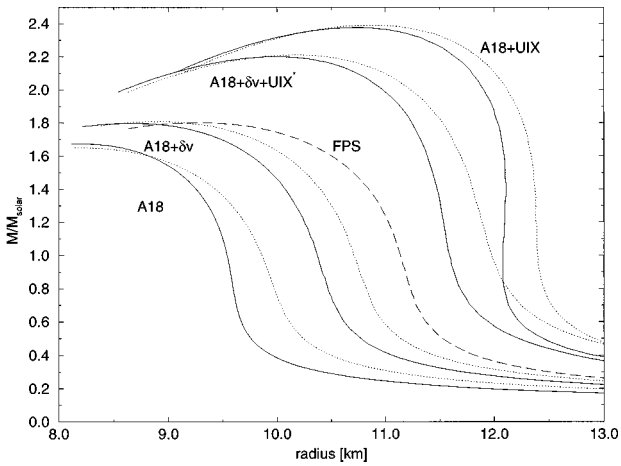

FIG. 12. Neutron star gravitational mass, in solar masses, vs radius, in kilometers, for the four models described in the text. The full curves are for beta-stable matter, and the dotted ones are for pure neutron matter. The dashed curve, FPS, is from [11].

TABLE XI. Maximum gravitational masses, in $M_\odot$, and moments of inertia I, in $M_\odot$ km^2, for stars with beta-stable matter and with PNM; with incompressible (INC) matter at $\rho > \rho_I$(fm^{-3}) for the A18+ δv +UIX* model; and with mixed nuclear-quark matter (NM+QM) phase (bag constant B in MeV fm^{-3}).

NM models	Max. mass beta-stable	Max. mass PNM	Max. I beta-stable	ρ_I of INC Models	Max. mass beta-stable	Max. I beta-stable
A18+ δv +UIX*	2.20	2.21	115	0.32	2.92	261
A18+UIX	2.38	2.39	143	0.48	2.46	157
A18+ δv	1.80	1.81	67	0.64	2.26	123
A18	1.67	1.68	55	0.86	2.19	115
FPS	1.80		73			
NM+QM models	B	Max. mass beta-stable	Max. I beta-stable	B	Max. mass beta-stable	Max. I beta-stable
A18+ δv +UIX*	122	1.91	96	200	2.02	107
A18+ δv	122	1.74	66	200	1.76	67

which is not far beyond the calculated VCS energies, so that only slight numerical extrapolation is involved.

The moments of inertia given in Table XI are the maximum values for each model. They occur for slightly lower central densities than do the maximum masses. The effect of the three-nucleon interactions on the maximum moment of inertia is in general considerably greater than on the maximum masses, because TNI tend to increase stellar radii also.

The relativistic correction to the Fermi energies, $-3k_F^4/56m^3$, mentioned at the end of Sec. III B, when inserted (with its attendant contributions to chemical potentials and pressure) into the EOS of the model A18+ δv +UIX*, produces at $\rho = 0.1$ fm^{-3} a reduction in pressure of 6.9%, but at $\rho = 1.0$ fm^{-3} the reduction is only 1.1%. The effect on the maximum mass is a 0.2% reduction, smaller than the digits quoted in Table XI.

The mass limits obtained with PNM EOS are within $\sim 0.5\%$ of the values determined from the EOS of matter in beta equilibrium, and the radii are within $\sim 5\%$. Thus the uncertainties in the proton fraction of matter discussed in the last section do not have a large effect on these aspects of neutron star structure.

A. Superluminality and maximally incompressible matter

Indicated on the curves in Fig. 11 are the densities ρ_{sl} at which the sound speed $c_s = \sqrt{\partial P/\partial \tilde{\rho}}$ becomes greater than the speed of light, c. Superluminal behavior would not occur with a fully relativistic theory, and it is necessary to gauge the magnitude of the effect it introduces at the higher densities. Kalogera and Baym [52] provide one method for doing this. Following Rhoades and Ruffini [53], they assume that the stiffest physically allowable EOS produces matter with a sound speed equal to the speed of light, i.e.,

$$\frac{\partial P}{\partial \tilde{\rho}} = c_s^2 \rightarrow c^2. \tag{5.2}$$

Since the matter is at zero temperature, for a single phase the partial derivative becomes a total derivative. Thus for higher densities than some $\tilde{\rho}_I$ the EOS is replaced by

$$P(\tilde{\rho}) = P(\tilde{\rho}_I) + (\tilde{\rho} - \tilde{\rho}_I)c^2, \tag{5.3}$$

and the matter interior to $\tilde{\rho}_I$ is then maximally incompressible. Other thermodynamically related quantities may be obtained easily [26]; the corresponding baryon number density is

$$\rho = \rho_I \sqrt{\frac{\tilde{\rho} + \frac{1}{2}(P_I - \tilde{\rho}_I c^2)}{\tilde{\rho}_I + \frac{1}{2}(P_I - \tilde{\rho}_I c^2)}}. \tag{5.4}$$

The relatively small reduction in the energy of the A18 + δv +UIX* model resulting from this replacement for $\rho_I = \rho_{sl} = 0.86$ fm^{-3} is shown in Fig. 13. In Fig. 14 we show the effect on the mass vs radius plot. The maximum mass is reduced from $2.20 M_\odot$ to $2.19 M_\odot$, a very small change. In all models of the present work superluminal behavior occurs in stars only very close to the maximum mass limit, as can be

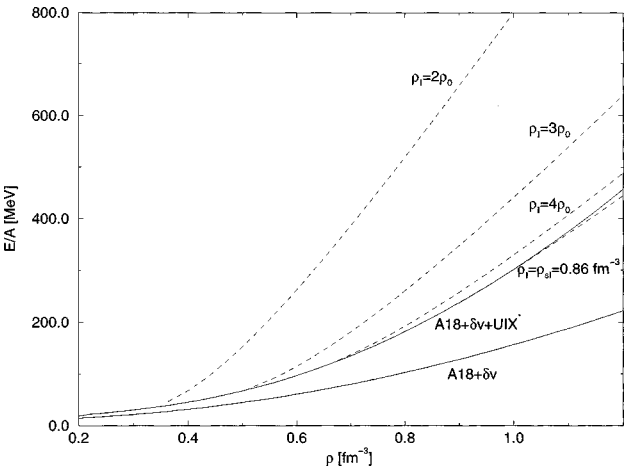

FIG. 13. For beta-stable matter according to the A18+ δv +UIX* model, the total energy per baryon vs baryon density (full curve). The dashed curves are for the assumption that matter is maximally incompressible for densities greater than the indicated value, and the lower full curve is for the A18+ δv model.

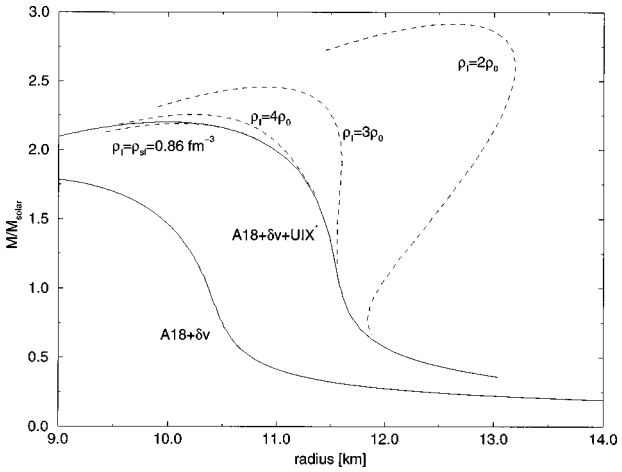

FIG. 14. Neutron star gravitational mass, in solar masses, vs radius for the A18+ δv + UIX* model (upper full curve), for the maximally incompressible modifications of this model at densities beyond chosen values of ρ_I (dashed curves), and for the A18+ δv model (lower full curve).

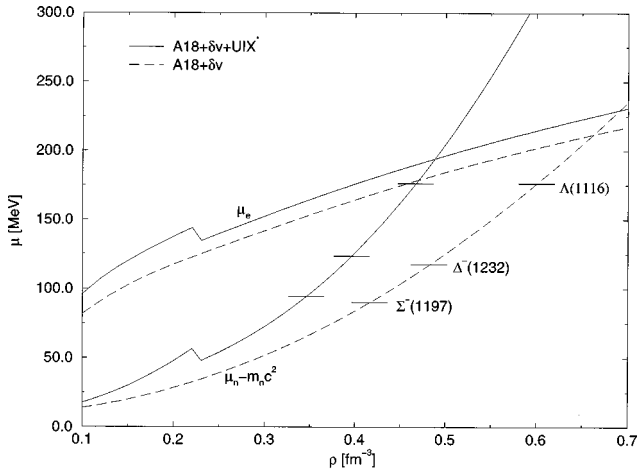

FIG. 15. The neutron and electron chemical potentials in beta stable matter according to models A18+ δv + UIX* (full line) and A18+ δv (dashed line). Threshold densities for the appearance of noninteracting hyperons are marked by horizontal line segments.

seen from Fig. 11. Therefore replacing superluminal matter with maximally incompressible matter has little effect on the stellar properties.

It is also possible that due to neglect of four-body and higher forces, and relativistic corrections of order (velocity)^4 and higher, the present work underestimates the sound velocity at lower densities. The effects of this possibility can be studied by assuming that the EOS of the A18+ δv + UIX* model is valid up to a chosen density ρ_I, beyond which it is maximally incompressible. The results obtained for $\rho_I = 2, 3,$ and $4\rho_0$ are shown in Figs. 13 and 14, and Table XI. The difference between the $E(\rho)$ of the matter obtained by assuming that $\rho_I = 2\rho_0$ and the $E(\rho)$ of the A18+ δv + UIX* model is several times the contribution of the UIX* interaction (see Fig. 14). It therefore appears unrealistic to assume that ρ_I can be as small as $2\rho_0$. Results obtained with $\rho_I = 3\rho_0$ provide a better indication of what we can expect from the hardest EOS consistent with realistic models of nuclear forces.

B. Transition to quark matter

It is also possible that the present EOS is too hard due to the assumption that neutron star matter contains only nucleons and leptons. Should it also contain other hyperons such as Λ, $\Sigma^{-,0,+}$ and $\Delta^{-,0,+,++}$, the EOS may be softer than that obtained with nucleons only [4]. The forces between hyperons and nucleons and between hyperons are not as well known as nuclear forces, and it is therefore difficult to estimate whether such exotic species are present in neutron star matter.

The chemical equilibrium in matter containing nucleons, lambdas, sigmas, deltas, and leptons is governed by the equations

$$\mu_{\Sigma^-} = \mu_{\Delta^-} = \mu_n + \mu_e , \tag{5.5}$$

$$\mu_\Lambda = \mu_{\Sigma^0} = \mu_{\Delta^0} = \mu_n , \tag{5.6}$$

$$\mu_{\Sigma^+} = \mu_{\Delta^+} = \mu_p = \mu_n - \mu_e , \tag{5.7}$$

$$\mu_{\Delta^{++}} = \mu_n - 2\mu_e . \tag{5.8}$$

If we neglect the interaction between nucleons and these hyperons, then the chemical potential of a hyperon at threshold density is given by its mass. Under such an assumption, the negatively charged hyperons appear in the ground state of dense matter when $\mu_n + \mu_e$ reaches their mass, while the neutral hyperons appear when μ_n equals their mass. Since μ_e in dense matter is larger than the mass differences between lambdas, sigmas, and deltas, the Σ^- and Δ^- will appear at lower densities than the neutral Λ, provided the interaction effects are small. The chemical potentials of electons, and of neutrons in beta-stable matter, are shown in Fig. 15 for the A18+ δv + UIX* and A18+ δv models. The threshold densities for noninteracting Σ^-, Δ^-, and Λ are indicated by horizontal line segments. Given their relatively low values, it is clear that in the absence of interactions these particles would be present in most neutron stars. Results obtained using crude models of the interactions between hyperons and nucleons, and between hyperons [4] indicate that the Σ^- and Δ^- have the largest effect of all hyperons on the EOS; however the magnitude of the effect is very sensitive to the interaction model.

The available hyperon-nucleon scattering data has been reviewed recently by de Swart, Maessen, and Rijken [54,55] along with the status of one-boson exchange models of the interactions between hyperons. Additional information on Λ-nucleon interactions can be obtained from the measured Λ-nucleus binding energies. These indicate the presence of ΛNN three-body forces that are as strong as the three-nucleon interaction [56,57]. In view of these uncertainties, particularly concerning the important Σ^- and Δ^- interactions, we do not attempt to estimate the effect of these hyperons on the EOS of neutron star matter.

A transition from hadronic to quark matter is expected at high densities. Knowledge of the EOS of both hadronic and quark matter is necessary to estimate the possible effects of this transition on neutron stars. Here, we use the present models of the EOS of hadronic matter, containing only nucleons and leptons, and the quark bag model with $u, d,$ and

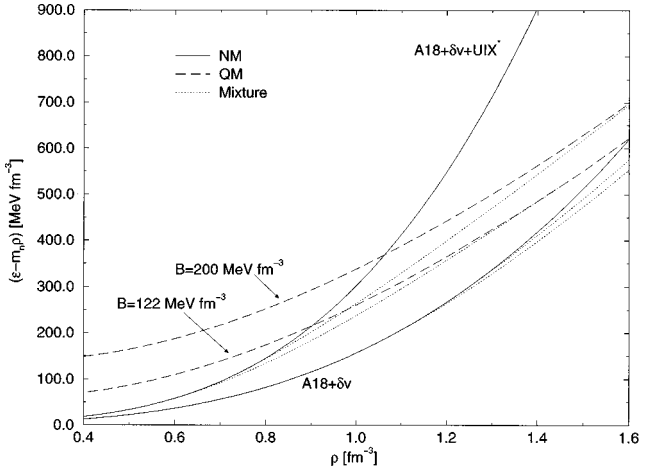

FIG. 16. For beta-stable matter, the energies per unit volume for the A18+ δv + UIX* and the A18+ δv models, and the quark bag models with $B=122$ and 200 MeV/fm^3 are shown by full and dashed lines; the dotted lines correspond to neutral mixtures of charged nuclear and quark matter.

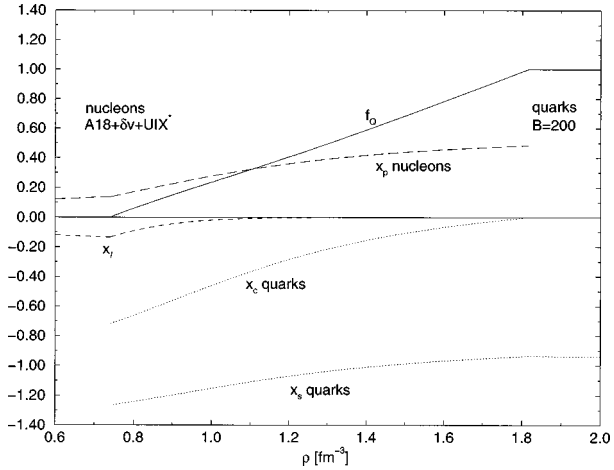

FIG. 17. For the A18+ δv + UIX* models and the quark bag model with $B=200$ MeV/fm^3, the proton fraction of nucleon matter x_p, the charge (x_c) and strangeness (x_s) per baryon of quark matter, the volume fraction f_Q occupied by quark matter, and the charge x_ℓ per baryon carried by the leptons in the mixture.

s quarks for the quark matter. The u and d quarks are taken to be massless, and s quarks to have a mass of 150 MeV. A Fermi gas of quarks of flavor i has density $\rho_i = k_{Fi}^3/\pi^2$, due to the three color states. There is no one-gluon exchange interaction energy between quarks of different flavor, while that between quarks of flavor i is given by $(2\alpha/3\pi)E_i$ per quark i [58]. Here E_i is the average kinetic energy per quark, and α is the strong interaction coupling constant, assumed to have a value of 0.5. The value of the bag constant B is poorly known, and we present results using two representative values of $B=122$ MeV [59] and $B=200$ MeV fm^{-3} [60].

The beta equilibrium conditions for charge neutral quark matter are

$$\mu_u + \mu_e = \mu_d = \mu_s, \quad \mu_\mu = \mu_e. \tag{5.9}$$

The energy densities of charge neutral quark matter and nuclear matter are plotted in Fig. 16. In the interesting region of $\rho \sim 1$ fm^{-3} the total energy density of quark matter is about 1200 MeV fm^{-3}, of which only 122 or 200 MeV fm^{-3} comes from the bag.

If, during the phase transition from nuclear to quark matter, the nuclear and the quark phase are each required to be charge-neutral beta-stable fluids whose pressures and baryon chemical potentials are equilibrated, then for the A18+ δv + UIX* model the transition is found to extend over the density range $\rho = 0.86 \leftrightarrow 1.57$ fm^{-3} for the $B = 200$ MeV fm^{-3} case. For $B=122$ MeV fm^{-3}, the range is $0.79 \leftrightarrow 1.20$ fm^{-3}. The matter within this density range, as so treated, is a constant-pressure mixture of that at the two ends of the range. Such a constant-pressure mixed phase does not occur in the neutron star: as can be seen from Eq. (5.1), since the pressure does not change, the density changes discontinuously from the lower nuclear matter density to the higher quark matter density.

Since for the nuclear component of the matter at $\rho \sim 1$ fm^{-3} the electron screening length is ~ 7 fm, while the quark matter component has negligible electron distribution, the previous assumption that each fluid retains its electron distribution during the phase-mixing is not a good approximation at length scales $\lesssim 7$ fm. As described in Ref. [23,26], an alternative assumption that the nuclear and the quark matter share a common electron distribution in the mixture is more appropriate. For a given nucleon matter density ρ_N the transition now involves equilibrating the chemical potentials,

$$\mu_n = \mu_u + 2\mu_d, \quad \mu_p = 2\mu_u + \mu_d, \tag{5.10}$$

and the hadronic pressures of nuclear and quark matter. In the process, the proton fraction of the nucleon matter and the densities of the quarks are also determined. The lepton chemical potentials are then given by

$$\mu_e = \mu_\mu = \mu_n - \mu_p = \mu_d - \mu_u, \tag{5.11}$$

from which the electron and muon densities are readily found. The fractional volume, f_Q, occupied by the quark component in the mixture is now chosen so that the nuclear, quark, and lepton components are in sum charge neutral:

$$\rho_e + \rho_\mu = \frac{1}{3} f_Q(2\rho_u - \rho_d - \rho_s) + (1 - f_Q)\rho_p, \tag{5.12}$$

after which the macroscopic baryon density of the mixture can be calculated:

$$\rho = \rho_{mix} = \frac{1}{3} f_Q(\rho_u + \rho_d + \rho_s) + (1 - f_Q)\rho_N. \tag{5.13}$$

The procedure is carried out provided that $0 \leqslant f_Q \leqslant 1$. Some numerical details are given in Appendix C.

The mixture of A18+ δv + UIX* model nucleon and the $B=200$ MeV fm^{-3} quark matter occurs over the density range $\rho_{mix} = 0.74 \leftrightarrow 1.80$ fm^{-3}. Over this range, a charge neutral mixture of quark and nucleon matter is more stable than the constant-pressure mixture of separately neutral nuclear matter and quark matter. The quark matter fraction f_Q, the charge per baryon of the nucleon matter, given by

the proton fraction x_p, the charge, x_c, and strangeness, x_s, per baryon of the quark matter and the charge x_ℓ per baryon carried by the leptons in the mixed matter are plotted for this case in Fig. 17.

Over the density range occupied by the mixture the nucleon matter has densities $\rho_N = 0.74 \leftrightarrow 0.96$ fm^{-3}, while the quark matter densities are $1.12 \leftrightarrow 1.82$ baryons fm^{-3}. The mixture thus consists of dense negatively charged quark matter immersed in somewhat less dense positively charged nucleon matter. The neutralizing charge of the leptons decreases in magnitude from its value in the purely nucleon matter, and tends rapidly to zero by the time the quark fraction has reached 50%.

The lower density end of the mixed phase region is more relevant for neutron stars. Here one expects small drops of dense quark matter with $x_c \sim x_s \sim -1$ appropriate for matter made up of Σ^- hyperons. Ground states of dense matter can have such a form also if matter made of Σ^- has a softer EOS than nucleon matter. Knowledge of the interactions between Σ^- hyperons is necessary to further explore this possibility. In regard to the direct Urca cooling process, the proton fraction of the nucleon matter in the mixture increases with f_Q, but the lepton fraction decreases. The required momentum balance among neutrons, protons, and electrons is only achieved at a baryon density of 0.86 fm^{-3}, somewhat larger than the value 0.78 fm^{-3} needed for the nucleon matter alone. At densities larger than 0.86 fm^{-3} the momentum balance remains possible, although the decreasing density of electrons reduces the rate of the Urca process. Thus the indirect effect of the quarks on the nucleons is to delay the start of the Urca process somewhat. At a density of 0.86 fm^{-3} the quarks, which are about 7% of the matter, can if behaving as free particles contribute to the Urca process directly. Such considerations, however, are complicated by effects of quark matter occurring as droplets.

At the high density end of the mixed phase, the quark matter has approximately equal number of u, d, and s quarks, and nearly symmetric nucleon matter occupies a small fraction of the total volume. Here one expects small drops of SNM, i.e., nuclei compressed to a density of $\sim 6\rho_0$ by the pressure of surrounding quark matter. However, this interesting form of matter at very large densities does not seem to occur in stable neutron stars according to the present calculations.

The two-component equilibrium suggested in Ref. [23] is formally the same as the equilibrium between nuclear matter and dripped neutrons in crustal neutron-star matter. Extending that similarity, Ref. [24] includes the effects on the phase transition of the energy of the surface dividing nucleon and quark matter, as well as the Coulomb energy associated with the difference between the charge densities of nucleon and quark matter. The lowest energy states of matter in the mixed region are then found to contain varying sizes and shapes of liquid in one phase surrounded by the liquid in the other phase. The presence of a new parameter of unknown magnitude, the surface energy, complicates the problem, however, and lacking new information on it, we have not included surface and Coulomb effects in results given here.

The energy densities of the mixed region, calculated neglecting its surface and Coulomb contributions, are shown in Fig. 16. As discussed at length in Ref. [23], the total pressure

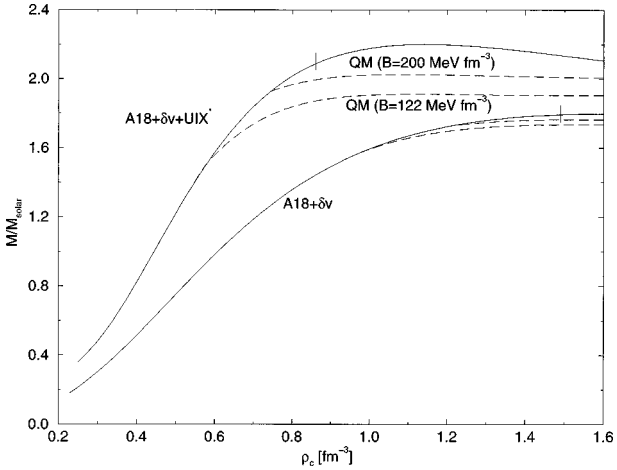

FIG. 18. Neutron star gravitational mass, in solar masses, vs central baryon density, for the A18$+\delta v+$UIX* and A18$+\delta v$ models with (dashed curves) and without (solid lines) quark matter admixture. The two dashed curves for the A18$+\delta v$ model are for $B = 122$ and 200, respectively.

obtained is now not constant over the density range of the mixture, although as can be deduced from Fig. 16, it is reduced from that of the pure nuclear matter. The resulting neutron star masses are shown in Fig. 18 as a function of central baryon density. Maximum masses are given in Table XI. For the A18$+\delta v$ model, admixing quark matter has small effects on neutron star structure; however, the effects are noticeable for models containing three-nucleon forces. Note that by neglecting the surface and Coulomb energies we underestimate the energy density of mixed matter and thus overestimate the effect of the admixture. The maximum densities in stable neutron stars remain below those for pure quark matter in all the four cases considered.

C. Transition to spin-ordered phase

When each phase is required to be charge neutral, the mixed region between the normal nuclear matter LDP and the spin-ordered, or neutral pion condensed HDP has constant pressure and constant average nucleon chemical potential. In the neutron star such a mixed region would not occur, and the density at this pressure would change discontinuously by 0.033 fm^{-3} for the A18$+\delta v+$UIX* model, a 15% jump. However, we should use the approach described in the last subsection for this transition also, and consider mixtures of charged LDP and HDP in a common lepton sea. On applying the equilibrium conditions of nuclear pressure and neutron and proton chemical potentials between the LDP and HDP, one finds that the density limits between which a mixture occurs is only slightly extended compared to those with the charge-neutral-fluid equilibrium quoted earlier, but the mixture does now have a pressure that changes with density. However, due to the similarity in charge character of the two phases the change in pressure in going from pure LDP to pure HDP is rather small, and therefore the thickness of the LDP-HDP mixed region in the star is also fairly small.

Selected neutron star density profiles for the A18$+\delta v+$UIX* model are shown in Fig. 19. Although it is not detectable from the figure, the mixed region associated with pion condensation now extends over a finite region of the

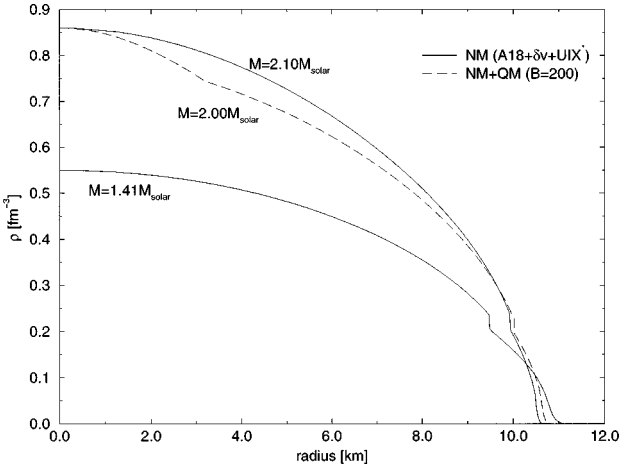

FIG. 19. Density profiles of $2.1M_\odot$ and $1.41M_\odot$ stars of beta-stable matter using the A18+ δv + UIX* model without quark matter admixture (solid lines), and of $2.00M_\odot$ star with quark matter admixture (dashed line), assuming a bag constant $B = 200$ MeV fm^{-3}.

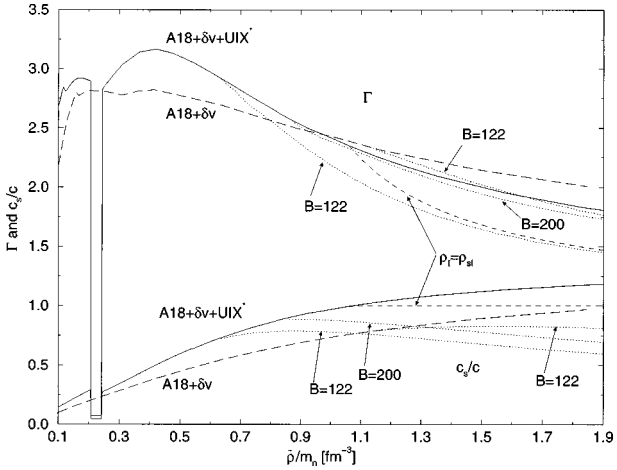

FIG. 20. The sound speed and the adiabatic index Γ vs $\tilde{\rho}/m$ for beta-stable matter according to the A18+ δv + UIX* (solid curves) and A18+ δv (long dashed curves) models. The short dashed curves are for the assumption that matter is maximally incompressible for densities greater than the indicated value. The dotted curves are for the nucleon-quark mixed phase.

star. Its radial thickness, Δr_T, is $\sim$14 m for the $2.10M_\odot$ case, and $\sim$40 m for the $1.41M_\odot$ case. The 2.10 and $2.00M_\odot$ stars shown in Fig. 19 have the same central density of 0.86 fm^{-3}; their mass difference is due to the admixture of quark matter considered only in the 2.00 $M_\odot$ star. The 1.41 $M_\odot$ stars cannot have quark matter admixtures in the present models.

It is interesting to know the structure of matter having a mixture of LDP and HDP. One possibility is that suggested for the nuclear matter-quark matter transition by Heiselberg, Pethick, and Staubo [24], that there occur in the mixed region varying sizes and shapes of matter in one phase surrounded by liquid in the other phase. If we apply their estimates to this phase transition, assuming a surface tension for the interface in the range $\sigma = 1$ to 10 MeV fm^{-2}, we find that the characteristic length scale a of the entities involved is $\sim$60 to 120 fm. The electron screening length, which for this approximation to be valid needs to be also of this magnitude, is only $\sim$10 fm, however. This indicates that neither assumption about the mixture, that of two charge-neutral fluids (which results in $\Delta r_T = 0$) nor of two nuclear components with a common electron fluid (which gives the Δr_T values given above) is correct, and we need to look at a mixture that is somewhere in between these extremes. That problem will be pursued elsewhere.

VI. ADIABATIC INDEX Γ OF NEUTRON STAR MATTER

A measure of the stiffness of matter described by the EOS $P = P(\tilde{\rho})$, is the adiabatic index Γ:

$$\Gamma = \frac{\tilde{\rho}}{P}\frac{\partial P}{\partial \tilde{\rho}} = \frac{\tilde{\rho}}{P}c_s^2 . \tag{6.1}$$

If Γ were constant, then the EOS would become $P \propto \tilde{\rho}^{\Gamma}$. In this form, it is called a *polytrope*, an idealized EOS on which many pioneering studies of stellar structure were based [61]. The values of Γ in several limiting cases are well known. At lower densities, the rest mass of the constituents dominates the energy density of matter, i.e., $\tilde{\rho} \approx \rho m$. In this limit, for matter without correlations, $\Gamma = 5/3$, 2, or 3 when the pressure is provided by Fermi kinetic energy, static two-body or three-body interactions, respectively. Repulsive momentum dependent interactions lead to larger values of Γ. In the opposite extreme of very high density, the energy per particle is much larger than the particle's rest mass. Neglecting rest mass, it is given by $\lambda\rho^n$, where $n = 1/3$, 1, or 2 for the above three cases, and λ is a constant. Thus $\tilde{\rho} = \lambda\rho^{n+1}$, $P = n\lambda\rho^{n+1}$, and $\Gamma = 1$ for all values of n. This does not contradict the well-known value of $\Gamma \to 4/3$ in white dwarfs [61]. In white dwarf matter the nuclei are nonrelativistic and the electrons are relativistic. The energy density of this matter $\tilde{\rho}c^2 = \rho M c^2$, where ρ is the number density of nuclei, and M is their mass. The pressure given by relativistic electrons is proportional to $\rho^{4/3}$ or equivalently $\tilde{\rho}^{4/3}$, giving $\Gamma = 4/3$.

Plots of Γ and the sound speed for various cases previously described are given in Fig. 20. The two curves corresponding to pure nucleons behave as expected from the above limits. From the crust, Γ rises to $\sim$3: of the two maxima, the greater value corresponds to the model with the explicit three-body interaction UIX*; Γ then decreases at higher densities. The small peaks followed by cusps in these curves at $\tilde{\rho}/m \sim 0.15$ fm^{-3} mark the softening of the EOS due to the opening of the muon channel. The deep discontinuity in both Γ and c_s for the A18+ δv + UIX* model are due to the LDP-HDP transition. The indicated values $\Gamma = 0.075$ and $c_s/c = 0.045$ shown at the bottom of the declevity are averages resulting from the treatment of that transition in Sec. V C. (When treated in terms of a mixture of neutral fluids, in which case the pressure is constant, these quantities would be zero.)

It is simple to express in terms of c_s^2, the extent of the stellar radius Δr_T occupied by this phase transition from Eq. (5.1):

$$\Delta r_T \approx \frac{c_s^2}{\tilde{\rho} g_T}\delta\tilde{\rho}, \quad g_T \approx \frac{G m(r_T)\Lambda(r_T)}{r_T^2}, \tag{6.2}$$

where $\tilde{\rho}$ is an average quantity for the two phases, $m(r_T)$ is the mass interior to the radius r_T at which the transition ocurs, $\Lambda(r_T)$ is the redshift factor there, and $\delta\tilde{\rho}\approx\delta\rho m$ is the density range of the transition, given earlier. The gravitational acceleration g_T at the transition region is greater for the more massive star, and explains the trend of our values obtained from the star profiles.

The use of maximally incompressible matter beyond $\rho=\rho_{sl}$, occurring in Fig. 20 at $\tilde{\rho}_{sl}/m=1.06$ fm^{-3}, produces a sharp reduction in Γ. This modification produces so little effect on the stellar mass limits (shown in Fig. 13) because it occurs at a density close to the central density in the star with maximum mass. The curves corresponding to nucleon-quark mixed phases discussed in Sec.V D reduce Γ and c_s more gradually: for an ultrarelativistic quark gas $c_s=c/\sqrt{3}$, and the sound velocities of models with quarks are seen to be approaching that value. Note that the partial derivative involved in the calculation of Γ and the sound velocity of nucleon-quark mixed phases must be carried out holding the quark fraction f_Q constant.

VII. CONCLUSIONS

The results obtained with the modern A18 NNI for the gross properties of neutron stars, such as the mass limit and the radius of $1.4M_\odot$ stars, are not very different from those obtained from the earlier U14 and A14 models [12]. The main difference is that with A18 and A14 NNI there is the indication of the neutral pion condensation phase transition, while there is none with U14. However, the fact that A18 provides an exact fit to the NN scattering data while U14 does not weighs against the U14 results.

As is well known, the cooling of neutron stars is accelerated by pion condensation [47]. The detailed mechanism associated with the spin-ordered condensate that we find is as yet unexplored. In addition, we estimate that due to this phase transition, there may be regions in the star where the matter density changes rapidly over a ten meter distance scale. The matter in this thin layer of the star can have interesting structures on a ten Fermi length scale.

We find that inclusion of the relativistic boost correction, δv, to the NNI increases the mass limit from $1.67M_\odot$ to $1.8M_\odot$ without any TNI, while it is reduced from $2.38M_\odot$ to $2.20M_\odot$ upon inclusion of the Urbana models of TNI. The reduction occurs because the TNI needed to fit nuclear data have weaker repulsive parts after including δv. For the same reason, the effect of Urbana models of TNI on the mass limit is diminished from $0.71M_\odot$ to $0.4M_\odot$ when the δv is included. Note that these models of TNI have only two terms; the long range two-pion exchange term, and a short range term with no spin-isospin dependence. Their strengths are determined from the density of SNM and the triton energy. However the triton, which has isospin 1/2, is insensitive to the interaction between three neutrons. Improved models of TNI must consider data such as the binding energy of ^{8}He, which are sensitive to the interaction between three neutrons.

If the effective value of the bag constant B is larger than 122 MeV/fm^3 it appears that only the heaviest neutron stars may have small drops of quark matter in their interior. The quark composition of these drops is similar to that of aggregates of Σ^- hyperons. If the interaction of Σ^- with dense nucleon matter is not repulsive, there may exist Σ^- hyperons in nucleon matter at densities below the threshold for the appearence of quark drops. It is necessary to build $N\Sigma^-$ and $NN\Sigma^-$ interaction models to more fully explore this possibility.

Using maximally incompressible matter at high densities we find that the upper limit for the maximum mass consistent with nuclear data is $\sim 2.5M_\odot$; this is not far from the prediction of $2.21M_\odot$ of our A18+δv+UIX* model. The lower limit for the maximum mass is more difficult to establish due to the unknown interactions between hyperons and nucleons. It may be as low as 1.74 $M_\odot$ if the quark bag constant B has a value of ~ 122 MeV/fm^3, and if the three neutron interaction is not as repulsive as the Urbana model IX at high densities, even without admixture of hyperons in matter. Recently several authors [62–64] have argued that there are indications of the existence of neutron stars with $M\sim 2M_\odot$. If these are confirmed, then models without TNI will be ruled out. However, such a possibility is still the subject of active debate [65].

ACKNOWLEDGMENTS

The authors thank F. Arias de Saavedra, G. Baym, D. Markovic, C. J. Pethick, J. Wambach, and R.B. Wiringa for useful discussions. This work was supported by the U.S. National Science Foundation through Grant No. PHY 94-21309. VCS calculations of nucleon matter were performed on the Cray C90 at the Pittsburgh Supercomputing Center.

APPENDIX A: FORM OF EFFECTIVE HAMILTONIAN

The effective interactions (energy densities) that fit the models examined in the first part of the paper all have the form

$$\begin{aligned} H_{\rm eff}=&\left(\frac{\hbar^2}{2m}+(p_3+(1-x_p)p_5)\rho e^{-p_4\rho}\right)\tau_n \\ &+\left(\frac{\hbar^2}{2m}+(p_3+x_p p_5)\rho e^{-p_4\rho}\right)\tau_p \\ &+g(\rho,x_p=0.5)(1-(1-2x_p)^2) \\ &+g(\rho,x_p=0)(1-2x_p)^2, \end{aligned} \tag{A1}$$

where $\rho=\rho_n+\rho_p$, and at zero temperature

$$\tau_p=\frac{1}{5\pi^2}(3\pi^2\rho x_p)^{5/3},\quad \tau_n=\frac{1}{5\pi^2}(3\pi^2\rho(1-x_p))^{5/3}. \tag{A2}$$

The parameters defining the τ-dependent terms are the same for all of the models, and are given in the caption of Table XII. For the A18 and A18+δv models at all densities and for the LDP of models with TNI, the parametrization is

$$\begin{aligned} g_L(\rho,x_p=0.5)=&-\rho^2(p_1+p_2\rho+p_6\rho^2 \\ &+(p_{10}+p_{11}\rho)\mathrm{e}^{-p_9^2\rho^2}), \end{aligned} \tag{A3}$$

TABLE XII. Parameter values for effective Hamiltonian for different models. The parameters $p_3 = 89.8$ MeV fm^5, $p_4 = 0.457$ fm^3, and $p_5 = -59.0$ MeV fm^5 [see Eq. (A1)] are common to all four models. The dimensions of the parameters, involving MeV and/or powers of fm, can be worked out from Eqs. (A1), (A4), or (A5).

Model	p_1	p_2	p_6	p_7	p_8	p_9	p_{10}	p_{11}	p_{12}	p_{13}
A18+δv+UIX*	337.2	−382	−19.1	214.6	−384	6.4	69	−33	0.35	0
A18+UIX	328.8	−404.6	−34	217.5	−385.6	6.35	25.4	0	0.47	−0.9
A18+δv	281.0	−151.1	−10.6	210.1	−158	5.88	58.8	−15	−0.2	−0.9
A18	297.6	−134.6	−15.9	215.0	−116.5	6.42	51	−35	−0.2	0
Model	p_{14}	p_{15}	p_{16}	p_{17}	p_{18}	p_{19}	p_{20}	p_{21}		
A18+δv+UIX*	0	287	−1.54	175.0	−1.45	0.32	0.195	0		
A18+UIX	−452	217.1	−1.0	100.3	−1.19	0.32	0.2	−275		

$$g_L(\rho, x_p = 0) = -\rho^2 (p_{12}/\rho + p_7 + p_8\rho + p_{13} e^{-p_9^2\rho^2}), \tag{A4}$$

while for the HDP of models with TNI,

$$g_H(\rho, x_p = 0.5) = g_L(\rho, x_p = 0.5) - \rho^2 (p_{17}(\rho - p_{19}) + p_{21}(\rho - p_{19})^2) e^{p_{18}(\rho - p_{19})},$$

$$g_H(\rho, x_p = 0) = g_L(\rho, x_p = 0) - \rho^2 (p_{15}(\rho - p_{20}) + p_{14}(\rho - p_{20})^2) e^{p_{16}(\rho - p_{20})}. \tag{A5}$$

The values of the parameters are as given in Table XII.

APPENDIX B: MOMENT OF INERTIA OF A SLOWLY ROTATING STAR

We use the general relativistic equations for a slowly rotating star as described by Hartle [66]. The metric for the nonrotating star is

$$ds^2 = -e^{\nu(r)} dt^2 + e^{\lambda(r)} dr^2 + r^2 (d\theta^2 + \sin^2\theta\, d\phi^2). \tag{B1}$$

It involves the radial functions $\nu(r)$ and $\lambda(r)$. The Oppenheimer-Volkoff equations for the pressure $P(r)$, mass function $m(r)$ and $\Lambda(r)$ are given in Sec. V, and $\lambda(r) = \ln(\Lambda(r))$. The function $\nu(r)$ is defined by

$$\frac{d\nu}{dr} = \frac{2G(m + 4\pi r^3 P/c^2)\Lambda(r)}{r^2}, \tag{B2}$$

with the boundary condition $e^{\nu(R)} = 1/\Lambda(R)$, and there is also an equation for the rotational drag, $\bar{\omega}(r)$,

$$\frac{d}{dr}\left(r^4 j \frac{d\bar{\omega}}{dr} \right) = -4r^3 \frac{dj}{dr} \bar{\omega}. \tag{B3}$$

Here $j(r) = e^{-(\nu(r) + \lambda(r))/2}$; it has the boundary value $j(R) = 1$. In the limit of slow rotation, such that the angular velocity $\Omega \ll GM/R^2 c$, $\bar{\omega}(r)$ has the boundary condition $\bar{\omega}(R)/\Omega = 1 - 2GI/R^3 c^2$. I is the total moment of inertia, given by either of the integrals

$$I = -\frac{2c^2}{3G} \int_0^R r^3 \frac{dj(r)}{dr} \frac{\bar{\omega}(r)}{\Omega} dr = \frac{8\pi}{3} \int_0^R r^4 \left(\tilde{\rho} + \frac{P}{c^2} \right) \Lambda(r) j(r) \frac{\bar{\omega}(r)}{\Omega} dr. \tag{B4}$$

This set of equations, together with Eq. (5.1), is integrated from $r = 0$ to the value $r = R$ where the pressure becomes negligible, with a given equation of state $P = P(\tilde{\rho})$, and a central density $\tilde{\rho}(0)$ chosen to give the desired neutron star mass. One then has also the radius and, after satisfying the boundary conditions, the moment of inertia.

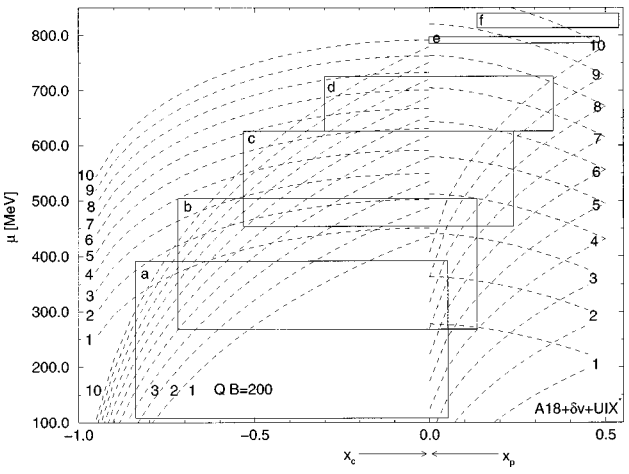

FIG. 21. Graphical representation of the strong interaction equilibrium between the A18+δv+UIX* model of nucleon matter and the $B = 200$ MeV quark matter for the density region of the mixing (see text). Dashed curves labelled 1 through 10 are strong interaction isobars, i.e., without considering charge effects and leptons. They are for pressures from 100 MeV fm^{-3} to 550 MeV fm^{-3} in intervals of 50 MeV fm^{-3}. The upper (lower) set of curves on the right side show the neutron (proton) chemical potential vs proton fraction (right side), and the quark-matter counterparts on the left side show $\mu_u + 2\mu_d$ ($2\mu_u + \mu_d$) vs charge per baryon x_c. The corners of the rectangles correspond to the equilibrium values of the chemical potentials and charge fractions.

APPENDIX C: DETAILS OF THE NUCLEON-QUARK EQUILIBRIUM

The nuclear matter-quark matter strong interaction equilibrium discussed in Sec.V B is illustrated graphically in Fig. 21. The $x_p > 0$ (right side) of the plot relates to nucleon matter and the left relates to quarks. Although states of quark matter can extend to $x_c = 2$ only the $x_c \lesssim 0$ part is relevant here. The chemical potentials of isobars corresponding to ten equally spaced pressures are shown as dashed lines. Equilibria corresponding to Eq. (5.10) and to pressure are represented by the rectangles. The top (bottom) horizontal sides of the rectangles join states with the same μ_n (μ_p) on quark and nucleon isobars corresponding to the same pressure. (Only in a few cases do the pressures involved correspond to those of the displayed grid.) The vertical sides ensure that the chemical potentials, μ_n and μ_p on nucleon side, and $2\mu_d + \mu_u$ and $2\mu_u + \mu_d$ on the quark side, belong to matter with the same charge per baryon. Other properties of interest, such as densities, are not represented on the plot. These equilibria are a property purely of the strong interactions, irrespective of leptons and charge neutrality. The latter property then determines the quark fraction f_Q, defined in Eq. (5.12). The rectangles labeled *b*, *c*, *d*, and *e* have values of f_Q going from 0.001 to 0.999 and represent physical states, while those labelled *a* and *f* give $f_Q = -0.169$ and $f_Q = 2.38$ corresponding to unphysical states. However, they all correspond to equilibrium under the strong interactions.

[1] See, for example, S. L. Shapiro and S. A. Teukolsky, *Black Holes, White Dwarfs, and Neutron Stars: The Physics of Compact Objects* (Wiley, New York, 1983).
[2] J. R. Oppenheimer and G. M. Volkoff, Phys. Rev. **55**, 374 (1939).
[3] S. E. Thorsett and D. Chakrabarty, astro-ph/9803260.
[4] V. R. Pandharipande, Nucl. Phys. **A178**, 123 (1971).
[5] H. A. Bethe and M. B. Johnson, Nucl. Phys. **A230**, 1 (1974).
[6] V. R. Pandharipande and R. B. Wiringa, Rev. Mod. Phys. **51**, 821 (1979).
[7] B. D. Day and R. B. Wiringa, Phys. Rev. C **32**, 1057 (1985).
[8] I. E. Lagaris and V. R. Pandharipande, Nucl. Phys. **A359**, 331 (1981).
[9] I. E. Lagaris and V. R. Pandharipande, Nucl. Phys. **A359**, 349 (1981).
[10] B. Friedman and V. R. Pandharipande, Nucl. Phys. **A361**, 501 (1981).
[11] C. P. Lorenz, D. G. Ravenhall, and C. J. Pethick, Phys. Rev. Lett. **70**, 379 (1993).
[12] R. B. Wiringa, V. Fiks, and A. Fabrocini, Phys. Rev. C **38**, 1010 (1988).
[13] R. B. Wiringa, R. A. Smith, and T. L. Ainsworth, Phys. Rev. C **29**, 1207 (1984).
[14] V. G. J. Stoks, R. A. M. Klomp, M. C. M. Rentmeester, and J. J. de Swart, Phys. Rev. C **48**, 792 (1993).
[15] V. G. J. Stoks, R. A. M. Klomp, C. P. F. Terheggen, and J. J. de Swart, Phys. Rev. C **49**, 2950 (1994).
[16] R. B. Wiringa, V. G. J. Stoks, and R. Schiavilla, Phys. Rev. C **51**, 38 (1995).
[17] R. Machleidt, F. Sammarruca, and Y. Song, Phys. Rev. C **53**, R1483 (1996).
[18] J. L. Friar, G. L. Payne, V. G. J. Stoks, and J. J. de Swart, Phys. Lett. B **311**, 4 (1993).
[19] L. Engvik, M. Hjorth-Jensen, R. Machleidt, H. Müther, and A. Polls, Nucl. Phys. **A627**, 85 (1997); M. Hjorth-Jensen (private communication).
[20] B. S. Pudliner, V. R. Pandharipande, J. Carlson, and R. B. Wiringa, Phys. Rev. Lett. **74**, 4396 (1995).
[21] A. Akmal and V. R. Pandharipande, Phys. Rev. C **56**, 2261 (1997).
[22] J. L. Forest, V. R. Pandharipande, and J. L. Friar, Phys. Rev. C **52**, 568 (1995).
[23] N. K. Glendenning, Phys. Rev. D **46**, 1274 (1992).
[24] H. Heiselberg, C. J. Pethick, and E. F. Staubo, Phys. Rev. Lett. **70**, 1355 (1993).
[25] J. D. Walecka, Ann. Phys. (N.Y.) **83**, 491 (1974).
[26] N. K. Glendenning, *Compact Stars* (Springer, New York, 1997).
[27] J. G. Zabolitzky, Phys. Rev. A **16**, 1258 (1977).
[28] Q. N. Usmani, B. Friedman, and V. R. Pandharipande, Phys. Rev. B **25**, 4502 (1982).
[29] R. B. Wiringa, Nucl. Phys. **A401**, 86 (1983).
[30] B. S. Pudliner, V. R. Pandharipande, J. Carlson, Steven C. Pieper, and R. B. Wiringa, Phys. Rev. C **56**, 1720 (1997).
[31] R. B. Wiringa, Nucl. Phys. **A361**, 70c (1998).
[32] H. A. Bethe and E. E. Salpeter, *Quantum Mechanics of One and Two Electron Atoms* (Academic Press, New York, 1957).
[33] F. Coester, S. C. Pieper, and F. J. D. Serduke, Phys. Rev. C **11**, 1 (1974).
[34] W. Glöckle, T.-S. H. Lee, and F. Coester, Phys. Rev. C **33**, 709 (1986).
[35] R. A. Krajcik and L. L. Foldy, Phys. Rev. D **10**, 1777 (1974).
[36] J. L. Friar, Phys. Rev. C **12**, 695 (1975).
[37] J. Carlson, V. R. Pandharipande, and R. Schiavilla, Phys. Rev. C **47**, 484 (1993).
[38] J. L. Forest, Ph.D. thesis, University of Illinois (1997).
[39] J. L. Forest, V. R. Pandharipande, J. Carlson, and R. Schiavilla, Phys. Rev. C **52**, 576 (1995).
[40] I. E. Lagaris and V. R. Pandharipande, Nucl. Phys. **A334**, 217 (1980).
[41] G. Q. Li, R. Machleidt, and R. Brockmann, Phys. Rev. C **45**, 2782 (1992).
[42] For a recent review of these topics, see C. J. Pethick and D. G. Ravenhall, Annu. Rev. Nucl. Part. Sci. **45**, 429 (1995); C. P. Lorenz, Ph.D. thesis, University of Illinois (1991).
[43] C. J. Pethick, D. G. Ravenhall, and C. P. Lorenz, Nucl. Phys. **A584**, 675 (1995).
[44] V. R. Pandharipande and D. G. Ravenhall, in *Proceedings of a NATO Advanced Research Workshop on Nuclear Matter and Heavy Ion Collisions, Les Houches*, edited by M. Soyeur *et al.* (Plenum, New York, 1989), p. 103.
[45] D. Vautherin and D. M. Brink, Phys. Rev. C **5**, 626 (1972).
[46] I. E. Lagaris and V. R. Pandharipande, Nucl. Phys. **A369**, 470 (1981).

[47] C. J. Pethick, Rev. Mod. Phys. **64**, 1133 (1992).
[48] G. E. Brown, C.-H. Lee, M. Rho, and V. Thorsson, Nucl. Phys. **A567**, 937 (1994).
[49] V. R. Pandharipande, C. J. Pethick, and V. Thorsson, Phys. Rev. Lett. **75**, 4567 (1995).
[50] R. B. Wiringa (private communication).
[51] H. Q. Song, M. Baldo, G. Giansiracusa, and U. Lombardo, Phys. Lett. B **411**, 237 (1997).
[52] V. Kalogera and G. Baym, Astrophys. J. Lett. **470**, L61 (1996).
[53] C. E. Rhoades and R. Ruffini, Phys. Rev. Lett. **32**, 324 (1974).
[54] J. J. de Swart, P. M. M. Maessen, and Th. A. Rijken, in *Properties and Interactions of Hyperons*, edited by B. F. Gibson, P. D. Barnes, and K. Nakai (World Scientific, Singapore, 1994), p. 37.
[55] Th. A. Rijken, Proc. of 6th Int. Conf. on Hypernuclear and Strange Particle Physics, Brookhaven (1997) (to be published).
[56] A. A. Usmani, S. C. Pieper, and Q. N. Usmani, Phys. Rev. C **51**, 2347 (1995).
[57] A. A. Usmani, Phys. Rev. C **52**, 1773 (1995).
[58] G. A. Baym and S. A. Chin, Nucl. Phys. **A262**, 527 (1976).
[59] J. Cleymans, R. V. Gavai, and E. Suhonen, Phys. Rep. **130**, 217 (1986).
[60] H. Satz, Phys. Lett. **113B**, 245 (1982).
[61] See, for example, S. Chandrasekhar, *An Introduction to the Study of Stellar Structure* (University of Chicago Press, Chicago, 1939).
[62] M. H. van Kerkwijk, P. Bergeron, and S. R. Kulkarni, Astrophys. J. Lett. **467**, L89 (1996).
[63] P. Kaaret, E. C. Ford, and K. Chen, Astrophys. J. Lett. **480**, L27 (1997).
[64] W. Zhang, T. E. Strohmayer, and J. H. Swank, Astrophys. J. Lett. **482**, L167 (1997).
[65] M. C. Miller, F. K. Lamb, and D. Psaltis, Astrophys. J. (in press).
[66] J. B. Hartle, Astrophys. J. **150**, 1005 (1967).